1-1-2006

Metastable production from electron impact dissociation of water, deuterium oxide, and hydrogen peroxide.

Xinqing Liao
University of Windsor

Follow this and additional works at: https://scholar.uwindsor.ca/etd

Metastable production from electron impact dissociation of H_2O (D_2O) and H_2O_2

By

Xinqing Liao

A Thesis
Submitted to the Faculty of Graduate Studies and Research
through Physics
in Partial Fulfillment of the Requirements for
the Degree of Master of Science at the
University of Windsor

Windsor, Ontario, Canada
2006

© 2006 Xinqing Liao

Canada

Abstract

The present work involves an investigation of the dissociation of H_2O, D_2O and H_2O_2 by electron impact over an incident energy range from threshold to 300eV. A pulsed electron beam, a target vapor beam, and the axes of detector were arranged to be perpendicular to each of others. By using channeltron detector, the fragments following the electron impact were probed so that the time-of-flight (TOF) spectra were obtained. In the case of H_2O/D_2O, significant isotopic effect was observed through comparison between TOF spectra for two targets. This isotopic shift was adopted to identify the fragments produced by dissociation of H_2O (D_2O). The major peak, which was thought to be due to the fragment only containing hydrogen (deuterium) element, in the TOF spectra was extracted and translated to total released kinetic energy (RKE) spectra. The excitation function for that peak was measured as well. At least three dissociation processes showed up, whose threshold were about 12.5eV, 23eV, and 58eV, respectively. In the case of H_2O_2, the TOF spectra were obtained, which, unfortunately, proved to be the mixture of TOF spectra for H_2O and for O_2. The possible reason for that is the much low vapor pressure of H_2O_2 relative to the vapor pressure of H_2O from the 30% water solution of H_2O_2. Further experiments are required to investigate the dissociation of H_2O_2.

Acknowledgements

I would like to thank my supervisor, Dr. W. Kedzierski, for the opportunity to work on this interesting experiment, for being a part of his laboratory, for the training he provided and for his patience. I am grateful to Mr. W. Qiu for his work in the laboratory. Thanks must go to many members of the physics department as well. Various parts of the apparatus were constructed by Mr. A. Jenner and Mr. E. Clausen. Mr. S. Jezdic provided superb electronic support. Without their superior work I would not achieve this thesis. The secretaries, Petrona Parungo and Marlene Bezaire, always provided help when I needed.

Appreciation goes to Mr.Haiping Sun for his selfless help. I also want to thank the Physics department for being my academic home for these years. Generous thanks go to my family and my friends for their enduring support and encouragement!

Table of Contents

List of Figures

vii

List of Abbreviations and Symbols

A .... Pulse amplifier [Figure 3.1]

BG .... Baratron gauge [Figure 3.1]

CE .... Collimation electrode [Figure 3.2, 3.3]

CF .... Cold finger [Figure 3.1]

CG .... Convectron gauge [Figure 3.1]

CH .... Channeltron detector [Figure 3.1]

cm .... Centimetre (unit of length)

CP .... Compressor [Figure 3.1]

CT .... Capillary tube [Figure 3.2]

CNDO .... Complete Neglect of Differential Overlap

CNDO/2 .... The main version of CNDO

D .... Discriminator [Figure 3.1]

DP .... Deflection plates [Figure 3.1]

EE .... Extraction electrode [Figure 3.2, 3.3]

EG .... Electron gun [Figure 3.1]

EID .... Electron impact dissociation

eV .... Electronvolt (unit of energy)

EX .... Expander [Figure 3.1]

F .... Filament [figure 3.3]

F .... Filter [Figure 3.1]

FB .... Filament bias supply [Figure 3.3]

viii

FC .... Faraday cup [Figure 3.1]

FH .... Filament holder [Figure 3.2]

FKE .... Fragment kinetic energy

FS .... Filament supply [Figure 3.3]

FWHM .... Full width at half maximum

IC .... Inner cup of faraday cup [Figure 3.2, 3.3]

K .... Kelvin (unit of temperature)

KHz .... Kilohertz (unit of frequency)

mA .... Milliampere (unit of electric current)

MC .... Master clock [Figure 3.1]

MCS .... Multichannel scaler/averager [Figure 3.1]

MHz .... Megahertz (unit of frequency)

mm .... Millimetre (unit of length)

MR .... Magnetic rod [Figure 3.2]

NIMs .... Nuclear instrumentation modules

nm .... Nanometre (unit of length)

NV .... Needle valve [Figure 3.1]

OC .... Outer cup of faraday cup [Figure 3.2, 3.3]

P .... Pulser [Figure 3.1]

PCHIP .... Piecewise cubic Hermite interpolation

pF .... Picofarad (unit of capacitance)

PMT .... Photomultiplier tube [Figure 3.1]

PRE .... Preamplifier [Figure 3.1]

ix

psi	pound-force per square inch (unit of pressure)
RKE	Released kinetic energy
S	Shutter [Figure 3.1]
s	Second (unit of time)
SR	Support rods [Figure 3.2]
TC	Thermocouple [Figure 3.1]
TOF	Time of flight
torr	millimetre of mercury (unit of pressure)
TP	Turbo pump [Figure 3.1]
uA	Microampere (unit of electric current)
uF	Microfarad (unit of capacitance)
us	Microsecond (unit of time)
V	Volt (unit of electric potential difference)
Ω	Ohm (unit of electrical resistance)
°C	Degree Celsius (unit of temperature)

Chapter 1

Introduction

Ancient Asians believed that water was a fundamental entity representing the source of everything on the planet. Today, as we know, liquid water is essential for life. 71 percent of the surface of our planet is covered with water. Water vapor evaporated from liquid water or ice represents a minor but environmentally significant constituent of the planetary atmosphere. The aurora, which is perhaps best known for its beautiful optical displays, happens when the accelerated charged particles (mostly electrons) in the solar wind collide with the atoms or molecules in the upper atmosphere. Finding out the complex physical significance behind this phenomenon is one of the motivations for the studies of electron-impact with particles, the scientific model of the aurora. As an important component of atmosphere, water was inevitably given much attention. In addition, lightning discharges lead to massive interaction between high-energy electrons and water vapor in the earth's lower atmosphere. Research of interaction of electrons with water vapor also has significance in some other fields, like radiation chemistry of water and radiation damage in tissue.

When water is subjected to the electron-impact dissociation there are produced atoms (H, O), molecules (H_2), radical (OH), and ions (H^+, H^-, O^+, O^{++}, O^-, OH^+, H_2^+) in their ground states and in various excited states. Most early investigations on the dissociation of water by electron impact have been made by observing the effects of

1

radiation of primary products. Vroom and de Heer [1] obtained the cross section data

for Lyman α and Balmer α, β, γ and δ emission at energies from 50 to 6000eV. Böse

and Sroka [2] determined appearance potentials and cross sections for excited

fragments with emission range of 500-1250A, and Beenakker et al. [3] measured

those with emission range of 1850-9000A. For the study of the translational

spectroscopy of excited hydrogen with short lifetime and no charges produced in

electron impact on water, Kouchi et al. [4] and Ogawa et al.[5] measured the Doppler

profiles of Balmer α and β lines. Lawrence [6] investigated the radiation of excited

atomic oxygen following electron impact of water vapor, specifically $O(3p^3P\text{-}3s^3S^0)$

and $O(3p^5P\text{-}3s^3S^0)$. Radiation of OH ($^2\Sigma\text{-}^2\Pi$) transition has been measured by

Hayakawa [7] and by Tsurubuchi et al. [8]. The latter work also included studies of

Balmer emission. Both direct and laser induced fluorescence techniques have been

introduced to monitor the production of OH [9,10,11].

The formation of ions in dissociation of water has also been the subject of

many investigations. Buchel'nikova [12] and Schulz [13] have shown that H^- is the

principal negative ion formed by electron impact in water relative to O^-. The

dissociative attachment cross sections H^- from H_2O and D^- from D_2O were reported

by Compton and Christophorou [14]. Dissociation ionization may occur in collision of

water molecules with electrons as well. Schutten et al. [15] have given partial and

gross ionization cross sections for the product ions H_2O^+, H^+, OH^+, H_2^+, O^+, and O^{++}.

The appearance potential of H^+ (D^+) and its kinetic energies also have been researched

by many workers [16,17,18]. The dissociative excitation of water by electron impact

2

has been reviewed by Olivero et al. [19]. Trajmar et al. [20] briefly summarized experimental techniques for measuring collision cross sections and exhibited a survey of the experimental cross section data.

Not only experimental works, but also relevant theoretical works have been performed for electron impact dissociation of water. A theoretical discussion of the direct formation of the hydrogen atom and the hydroxyl radical has been given by Niira [21,22]. By combining semiquantitative theoretical conclusion with experimental data, Laidler [23] discussed the mechanisms involved in the formation of ions during the interaction of water vapor with high-energy electrons. Leclerc et al. [24] used CNDO/2 method supplemented by configuration interaction calculation to investigate the symmetric dissociation of the H_2O^+ ions in the lower-lying states. A theoretical interpretation of the optical and electron scattering spectra of water has been given by Claydon et al. [25].

Although the optical studies were widely adopted for dissociation of water by electron impact, investigations of the metastable states are made difficulty by their long lifetime. Production of metastable fragment also has some advantages. Since metastable fragments could be directly detected, it is possible to measure the kinetic energy distribution and the angular distribution of dissociation metastable fragments that provide us significant information about corresponding excited states. The pioneer work for metastable fragment from dissociation of water was given by Clampitt [26] who reported the threshold and kinetic energy of metastable H(2s). Freund [27] extended the previous study on metastable fragments formed by electron

3

impact dissociation of water. In his work fragment H(2s), $H_2(c^3\Pi_u)$ and probably $O(^5S^0)$ were discussed. Kedzierski et al. [28] introduced novel solid xenon matrix detector that is selectively sensitive to $O(^1S)$, and kinetic energies and energy dependent cross sections of $O(^1S)$ fragment from H_2O and D_2O have been measured by them.

In present work, we attempt to use channeltron detector to probe the metastable productions of H(2s) (D(2s)) and $O(^5S)$ formed in electron impact dissociation of water and heavy water over an incident energy range from threshold to 300eV. A pulsed electron beam was cross-fired with the target molecule vapor beam to obtain time-of-flight (TOF) spectra, and therefore we are able to translate the TOF data into kinetic energy spectra of the detected fragment. Furthermore, by sweeping the voltage on electron gun filament, the relative cross sections as a function of impact electron energy were measured. Body of this work is organized as follows. Chapter 2 deals with the fundamental theoretical and experimental problems of dissociation. We briefly explain the dissociation process and the methods used in our experiment (eg., time-of-flight, and excitation function). The interpretation of experimental results builds on base of this background information. Chapter 3 shows our experimental apparatus. Each functional part of specific equipment is discussed in detail. Chapter 4 presents results for electron collisions with targets of water and heavy water. Isotope effect is employed to help identify the signals shown in our results.

Electron impact dissociation of hydrogen peroxide has been seldom discussed so far. Hydrogen peroxide (H_2O_2), like water (H_2O), is made up of elements of

4

hydrogen and oxygen. If the H_2O_2 vapor is taken as the target of incident electrons, the fragments formed in dissociation are supposed to be similar as fragments from H_2O. Although hydrogen peroxide looks like water with an extra oxygen atom, the physical properties of H_2O_2 are much different from those of H_2O. H_2O_2 contains a single bond between two oxygen atoms. The different geometrical molecule structure and band strength must lead to the different behaviors in the electron impact breakup from water. Desirability of exploring the phenomena of dissociation of H_2O_2 motivates us to involve the H_2O_2 as target in our work. Chapter 5 gives the results of our hydrogen peroxide investigation with a discussion of the possible dissociation process. Also, some suggestions are provided for the future work in Chapter 6. An appendix is attached to explain the calculation of the H_2O_2 vapor pressure evaporated from an aqueous solution of H_2O_2.

Chapter 2

Background Knowledge

The dissociation process

In physics, molecule dissociation is considered as a consequence of the molecule states transition that occurs from a bound state to a repulsive state (or to the repulse wall of a bound state). Change of the electron state of the molecule plays a very important role in this process. Molecule energy consists of the energy of electrons (kinetic energy and potential energy) and the energy of nuclei (kinetic energy and potential energy). The electronic energy is tied up with the internuclear distance r so that the change of the position of the nuclei causes not only the change of Coulomb potential of the nuclei but also the change of the electronic energy. Therefore, the electronic energy and the Coulomb potential of nuclei work together as the potential energy during the motion of nuclei. Consider a situation of diatoms molecule, the plot of effective potential energy (electronic energy + Coulomb potential) as a function of internuclear distance r is usually referred as potential curve. Since the electronic energy is discrete when r is fixed, the effective potential energies of a molecule are characterized by a series of potential curves that are called the electronic states of molecule. The curve with a minimum, whose position corresponds to equilibrium internuclear distance, is said to be a stable state (bound state). If the energy of molecule relative to the minimum is lower than the asymptote of the curve, the molecule will vibrate with respect to equilibrium. Conversely, the potential curve,

6

which as no minimum, is unstable. The two atoms repel each other at any internuclear distance. Figure 2.1 illustrates a bonding curve X and a repulsive curve Y.

Dissociation takes place when the target molecule is excited from a bound electronic state to a repulsive electronic state (or to the repulse wall of a bound state). It is very convenient to picture qualitatively the dissociation process by Franck-Condon principle, which states that the electron jump in a molecule takes place so rapidly in comparison to the vibrational motion that immediately afterwards the nuclei still have very nearly the same relative position and velocity as before the "jump". Let us apply this principle on two distinguished cases of dissociation under the hypothesis of diatoms molecule, as shown in Figure 2.1: (a) dissociation from a pure repulsive state, (b) dissociation from the repulsive well of a bound state.

Figure 2.1(a) shows process A, which is a rough model involving a bound and a repulsive potential curves. As indicated above, the lower curve X which represents the ground electronic ground state is a bound molecule state. Consider a diatomic molecule AB, AB is initially at the ground vibrational level (v=0, the straight line on bottom of curve X) of the state X with two classical turning points at r' and r''. The two vertical dashed line drawn through the turning points of the v=0 level define the Franck-Condon region. The ground vibrational wave function is characterized by the bell-shape curve on the bottom line (v=0 level) of curve X. The upper curve Y corresponding to an excited electronic state is repulsive, and the molecule AB separates into two parts A and B* for large internulear distance, where B* is a metastable B.

7
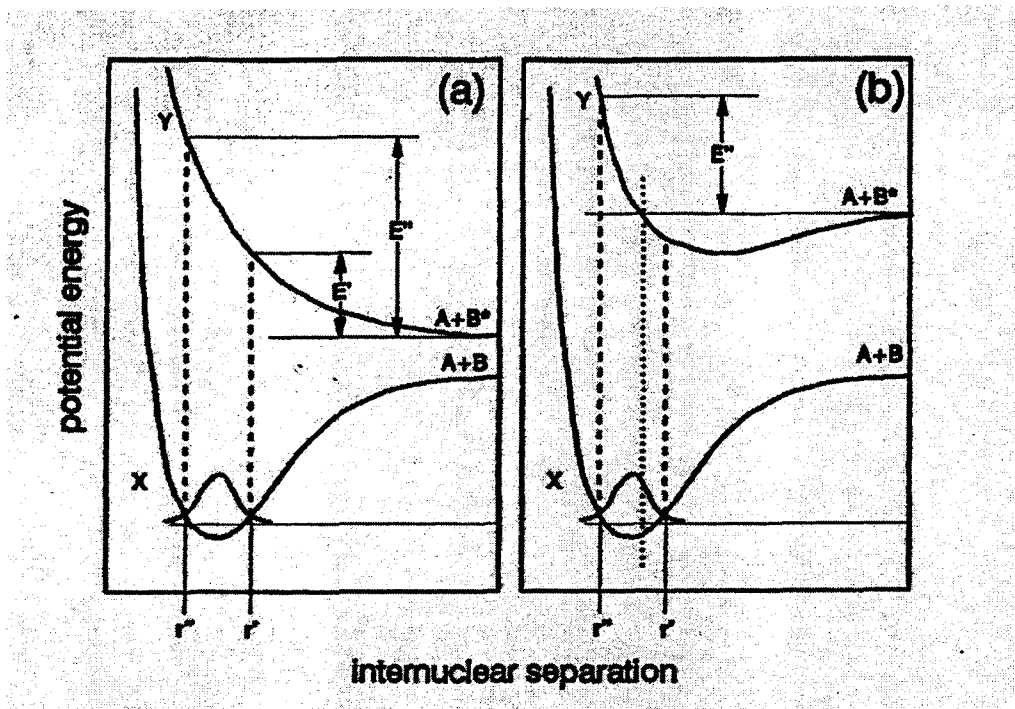
Figure 2.1. Potential energy curves for hypothetical diatomic molecule AB to illustrate (a) dissociation from a purely repulsive state, and (b) dissociation from the repulsive wall of a bound upper state.
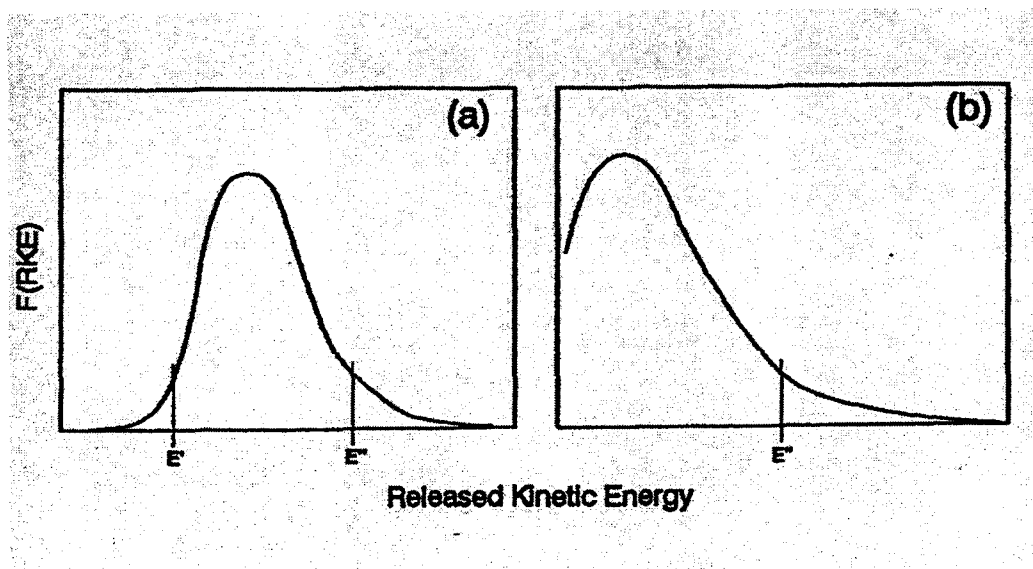
Figure 2.2. Released kinetic energy spectra for dissociation processes (a) and (b) in Figure 2.1.

8

During the collision, the molecules on the ground state are excited. According to the Franck-Condon principle, the transition only occurs vertically upward. The molecule at r' absorbs enough energy and jumps along the dashed line to the cross point on Y where the velocity of the nuclei are still zero at the moment. The molecule then splits into A and B* that fly apart with a released kinetic energy (RKE) E'. The molecule at r" follows the same process to break up with the RKE E".

Since the target molecule have a distribution with respect to internuclear distance, the RKE obtained become diffuse during the dissociation process. The RKE distribution is illustrated in Figure 2.2(a) and the positions of E' and E" are indicated. The shape of the distribution is approximately estimated by reflecting the X (v=0) nuclear wavefunction in the Franck-Condon region through the potential curve of upper state Y to the energy scale. The dissociations from a purely repulsive state always have an RKE distribution as shown in Figure 2.2(a).

In process B, the minimum of the upper potential curve lies at a still greater internulear distance than that of the lower curve. The vertical transition along the dotted line in the Franck-Condon region makes the molecule jump to a upper curve point that lies on the asymptote of curve and therefore break up into A and B* with zero released kinetic energy. The molecule in the right region of dotted line will be excited to some discrete bound vibrational levels in the potential well of the upper curve. Only in the left region of the dotted line dose the transition make dissociation happen. In this case, the excitation involves a transition from a ground state to a repulsive part of a bound state. The RKE distribution is shown in Figure 2.2(b). The

9

obvious difference from the last case is that it has a finite value at zero kinetic energy that depends on the relative position of the minima of the two curves.

Let us consider a situation that is a little complicated. The minima of the two bound states lie with one very nearly above the other. In general, the molecule is excited from ground state to the upper vibrational level without dissociation. However, if the upper bound state is overlapped by a repulsive state corresponding to the separation into atoms, there is a possibility of transition from the bound state to the repulsive state without radiation. In this case, the molecule excited to the upper bound state undergoes this radiationless transition to the repulsive state after a certain lifetime and thereby dissociation takes place. This process is called pre-dissociation.

Time-of-flight

The kinetic energy distribution of the fragment is one of important problems in the study of electron impact dissociation of molecule. For neutral metastable fragment, Time-of-flight is frequently employed to determine the energy distribution of particles in collision experiment. In practice, periodic electron pulses are used to measure TOF spectra. When the target molecules in the interaction region are excited by electron pulse, both dissociation process and photon emission take place. Prompt photons are captured by detector almost at the same time as pulse is on and taken as zero mark of time scale, while the fragments of dissociation take some time to fly to detector that is fixed with a distance of D from the interaction region. The distribution of the time

10

delays of the fragment $f(t)$ is called TOF spectrum. The kinetic energy distribution can be developed from TOF spectrum, which provides fundamental information on the repulsive states of the parent molecule.

If the mass of the detected metastable fragment is known or guessed, the fragment kinetic energy (FKE) is given by

$$T_{EF} = \frac{1}{2}m(D/t)^2. \qquad [2.1]$$

where t is time delay, D is the distance between detector and interaction region as indicated above. Let us consider distribution of FKE. No matter what kind of the distribution is taken into account, the total counts should be conserved. That means the area under any distribution should be a constant, then

$$\int f(t)dt = \int F(T_{EF})dT_{EF} \qquad [2.2]$$

If we take derivative on both sides of equation 2.2 and insert the expression of dt with respect to dT_{EF} into the left side of equation 2.2, we get (the minus sign is neglected)

$$F(T_{EF}) = \frac{t^3}{mD^2} f(t) \qquad [2.3]$$

Equation 2.3 represents the relationship between TOF spectrum and the distribution of FKE, which is characterized by t^3 factor.

By using the same procedure, the speed distribution $g(v)$ of the fragment can be determined by

$$g(v) = \frac{t^3}{D} f(t). \qquad [2.4]$$

In general, dissociation process is complicated. The parent molecule breaking

11

up into multiple fragments makes it quite difficult to derive the released kinetic energy (RKE) of the process. For the simplest case, we assume that only two fragments are produced after the collision. Since the total momentum is conserved, the RKE is related to the kinetic energy of fragment 1, by the following

$$T_{ER} = \frac{M}{m_2} T_{EF1} \tag{2.5}$$

where m_2 is the mass of fragment 2, and M is $m_1 + m_2$. Because of the conservation of total counts, the distribution of RKE is given by

$$\int F(T_{ER}) dT_{ER} = \int F(T_{EF}) dT_{EF} \tag{2.6}$$

$$F(T_{ER}) = \frac{m_2}{M} F(T_{EF1}) = \frac{m_2 t^3}{M m_1 D^2} f(t) \tag{2.7}$$

where m_2 is the mass of undetected fragment, and M represents the mass of the parent molecule. Now let us focus our attention on the term t^3 in the equation 2.7 and equation 2.4. This can lead to relatively extreme data scatter at low kinetic energy because of background present in experimental data. The RKE distribution can be viewed as a "reflection" of the ground state wavefunction of the nucleus on the repulsive potential curve.

In the case of polyatomic molecules dissociation, for example H_2O (or D_2O), the model we discussed above is still available if the parent molecule breaks up into two fragments. However, the potential energy states of the nuclei are no longer represented as curves, but as surfaces. During the dissociation process, the vibrational and rotational translations of the molecular fragments should be taken into account. The potential energy contributes not only to translational energy but also to

12

vibrational and rotational energy of the fragments. That makes it hard to rebuild the

repulsive potential surface from the released kinetic energy distribution.
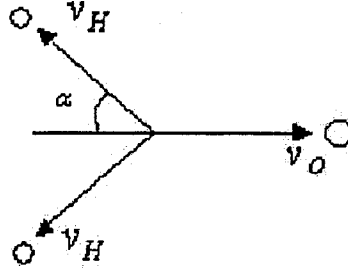
Figure 2.3 Symmetric three-body dissociation of water

For three-body dissociation, in our case $H_2O(D_2O) \rightarrow H(D) + H(D) + O$, the

conservation of momentum principle forms the foundation for the analysis of the

process. Figure 2.3 shows the situation of symmetric breakup of water. The relation

between momentum of hydrogen product and oxygen product is given by

$$m_o v_o = 2m_H v_H \cos\alpha \qquad\qquad [2.8]$$

where m_O and m_H represent the mass of hydrogen product and oxygen product

respectively, v_O and v_H represent the velocities of hydrogen product and oxygen

product respectively, and α is the angle between the direction of one of two

hydrogen products and the opposite direction of oxygen product. α varies from 0 to

$\pi/2$ but can not be equal to $\pi/2$. The total released kinetic energy is expressed as

$$T_{ER} = T_{EFO} + 2T_{EFH}$$

$$= \frac{1}{2}m_O v_O^2 + 2(\frac{1}{2}m_H v_H^2) \qquad\qquad [2.9]$$

where T_{ER} is total released energy, T_{EFO} and T_{EFH} are the kinetic energies of

13

oxygen product and hydrogen product, respectively. By substituting equation [2.8] into equation [2.9], we get

$$T_{ER} = T_{EFO}(1 + \frac{m_O}{m_H 2\cos^2 \alpha})$$ [2.10]

$$= 2T_{EFH}(\frac{m_H 2\cos^2 \alpha}{m_O} + 1)$$ [2.11]

It is clear that the equation [2.10] and equation [2.11] have a dependence of angle α. (Since the hydrogen product has the identical probability of fling away along the direction with any possible α, it is reasonable to just consider the average contribution of the all angle α.) The term $\cos^2 \alpha$ can be replaced by its average from 0 to $\pi/2$, which is 1/2, and then the equation [2.10] and equation [2.11] are reduced to

$$T_{ER} = T_{EFO}(1 + \frac{m_O}{m_H})$$ [2.12]

$$= 2T_{EFH}(\frac{m_H}{m_O} + 1)$$ [2.13]

Excitation functions.

In the previous section, we discussed the way of converting TOF distribution to released kinetic energy (RKE) distribution. As can be seen in Figure 2.4, the RKE is directly related to the molecular repulsive potential curve in the Franck-Condon region, but it is not the whole story of the repulsive state. Another data analysis process, excitation function, is usually employed in the TOF experiment to explore

14

the further features of the repulsive state. By repetitively sweeping the electron gun filament voltage, an excitation function can be obtained, which is a plot of the number of the incoming fragments as a function of electron impact energy. If all fragments, regardless of flight time, are accumulated against electron energy, the observed excitation function is a superposition of the contributions of all possible dissociation channels. Such excitation function curve may exhibit several sharp changes in slope (called breaks). The intercept of each slope on the energy axis corresponds to the appearance energy (threshold) energy of a particular metastable fragment. The change in slope indicates the existence of another appearance energy and thereby an additional dissociation channel.

In practice, excitation function is usually applied in a selected time window of TOF. In the other word, only the incident fragments arriving at detector in a set-up TOF interval are accumulated as a function of electron energy (called a windowed excitation function). Let us consider the situation of diatomic molecule dissociation as shown in Figure 2.4. The transition takes place between the bound state X and repulsive state Y and thus the molecule separate into A* and B* with released kinetic energy (RKE). The appearance energy also known as threshold is labeled as E_t. E_A and E_B represent the excitation energies of the metastable atoms A* and B*, respectively, resulting from curve Y. E_d means the dissociation energy of molecule AB that is in its ground vibrational state X(v=0) with respect to the separated atoms A and B in their ground states.

15
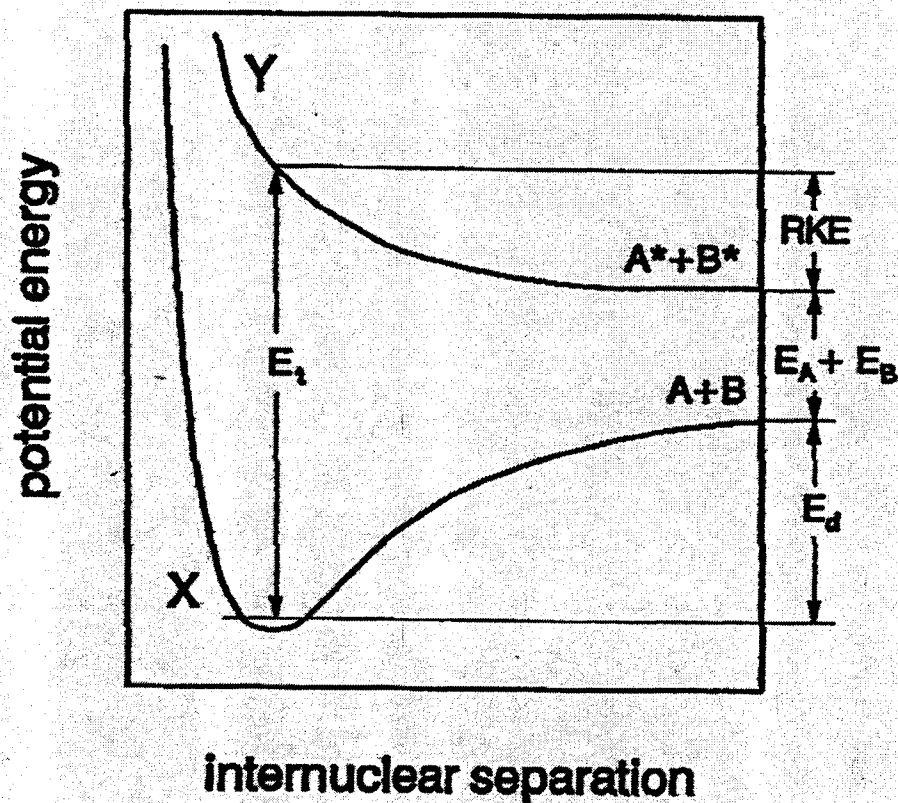
Figure 2.4. Illustration of internuclear potential energy curves for diatomic molecule AB and relevant quantities.

16

From the diagram, it is easy to see that

$$E_t = E_A + E_B + E_d + T_{ER} \qquad [2.15]$$

where, the dissociation limit is defined as

$$E_{dl} = E_A + E_B + E_d \qquad [2.16]$$

Recall that

$$T_{ER} = \frac{M}{m_2} T_{ER} \qquad [2.5]$$

By substituting equation [2.15] and equation [2.16] into equation [2.5], we can get

$$T_{EF1} = \frac{m_2}{M}(E_t - E_{dl}) \qquad [2.17]$$

The equation [2.17] illustrates a linear relationship between the FKE(T_{EF}) from the TOF spectra and the appearance energy. If the thresholds of several excitation functions for a set of time windows corresponding to various FKEs are measured, it is very useful to plot the FKEs against the thresholds for the range of TOF region which is expected to a straight line. In the case of uncertain fragement mass, the slope of the straight line, $\frac{m_2}{M}$, will be helpful to verify the mass assignment. This procedure was extensively discussed by Allcock and McConkey [29]. The intercept of the line on the threshold axis is the dissociation limit of the potential curve, E_{dl}. By using the dissociation limit and the minimum released kinetic energy together, the repulsive potential curve in the Franck-Condon region can be located. The excitation function techniques are also available for particular photon decay windows. The excitation function of H_α emission of hydrogen is used to calibrate the electron energy in this work.

17

Cross section

The cross section is a measure of the probability of the interaction between the incident electrons and the target molecules. That interaction leads to excitation of the molecules to repulsive state on which the molecules will dissociate into fragments. In practice, the cross section is not a constant, but depends on the collision energy. As mentioned previously, the excitation function is a plot of the fragment yield as a function of the electron impact energy. Since the count rate of a detected fragment is proportional to the cross section of the dissociation process, the excitation function is often called relative cross section from which we can learn how the cross section change with the various energies.

Consider a beam of electrons with intensity of I passing through a low-pressure molecular gas. The attenuation of the intensity due to collision with the target molecule, which is excited from a bound state ψ_0 to some repulsive state ψ_n accompanied by production of metastable fragment, is proportional to the number density of the target gas N, beam intensity I and the traveling distance dz. Thus, the expression of dI is given by

$$dI = -IN\sigma_n dz. \qquad\qquad [2.18]$$

The parameter σ_n, which has the dimensions of area, is called the cross section. The negative sign indicates the decrease of the beam intensity I. Suppose each collision release a metastable fragment. The electron beam intensity, therefore, decreases at the same rate as the metastable fragments are produced. dM symbolizes the emission

18

rate of metastable fragments, then

$$dM = IN\sigma_n dz \qquad\qquad [2.19]$$

It is well known that the beam intensity can be expressed as

$$I = N_e vdA, \qquad\qquad [2.20]$$

where N_e is the number density of electrons at the location of (x,y,z), v is the relative velocity of electron in the center of mass frame, and dA is the cross sectional area of the electron beam. If it is assumed that the metastable fragments are released equably in space, then the production of metastable fragments per second per unit volume per steradian is written as

$$\frac{dM(x,y,z)}{dVd\Omega} = \frac{1}{4\pi}N_e(x,y,z)N(x,y,z)v(x,y,z)\sigma_n. \qquad [2.21]$$

Note that the relationship of

$$dV = dzdA \qquad\qquad [2.22]$$

was used during the derivation. The integration of equation [2.21] over the collision region and solid angle of detector surface gives a theoretical estimate of the count rate of metatable fragment received by detector.

Usually it is almost impossible to calculate the electron impact cross section exactly, thus some approximate methods are introduced in the theoretical treatment of collision process. Some of those approaches will be discussed briefly in the following. (An atomic target gas will be considered for simplicity, but the discussion can equally be applied to molecules.)

Consider a process of collision between an incident electron with velocity of v and a stationary atom with mass of M. The atom is excited from an initial state

19

ψ_o to a final state ψ_n with the energy interval of E_n, and the electron is scattered into an infinitesimal solid angle $d\Omega$ along the direction with polar angle φ and θ measured in the center of mass frame. For higher collision energy, interaction between the electron and the target atom lasts for short time, and translations of the energy and momentum are expected to be small. This implies that the first Born approximation is appropriate for this high energy process. If the electron exchange effect is neglected, the differential cross section derived from Born approximation [30] is

$$d\sigma_n = \frac{\mu^2}{(2\pi\hbar^2)^2} \frac{k'}{k} \left| \int e^{i\vec{K}\cdot\vec{r}} \psi_n^* V \psi_o d\vec{r}_1, \cdots, d\vec{r}_z d\vec{r} \right|^2 d\Omega \qquad [2.23]$$

where $\mu = (m_e \cdot M)/(m_e + M)$ is the deduced mass of the colliding system, m_e i s the mass of the electron, $\vec{r}_1, \cdots, \vec{r}_z$ are the coordinates of the atomic electrons, Z is the number of atomic electrons, $\vec{r}$ is the coordinate of the colliding electron relative to the center of the atom, $\hbar\vec{k}$ and $\hbar\vec{k}'$ represent the momentum of the colliding electron before and after the collision respectively, and therefore $\hbar\vec{K} = \hbar(\vec{k} - \vec{k}')$ is the momentum transfer to the atom. V is the interaction potential between the colliding electron and target atom. When the Coulombic potential

$$V = -\sum_{j=1}^{z} \frac{e}{|\vec{r} - \vec{r}_j|} + \frac{Z_N e}{r} \qquad [2.24]$$

(where $Z_N e$ is the charges of the nucleus) is taken into account, the equation [2.23] transforms into

$$d\sigma_n = \frac{4m_e^2 e^4}{\hbar^4} \frac{k'}{k} \frac{1}{K^4} |\varepsilon_n(\vec{K})|^2 d\Omega \qquad [2.25]$$

where $\varepsilon_n(\vec{K})$ is the matrix element

20

$$\varepsilon_n(\vec{K}) = \left\langle \psi_n \left| \sum_{j=1}^{Z} e^{i\vec{K}\cdot\vec{r}_j} \right| \psi_o \right\rangle. \qquad [2.26]$$

Since the atomic mass is much heavier than electron mass, the electron mass can be safely inserted into the place of the reduced mass in the equation [2.25], and then the center of mass frame and the laboratory frame have negligible difference. The quantity of $d\sigma_n$ is axially symmetric around the incident direction because of the random atomic orientation. However, it depends on the scattering angle θ by $K = (k^2 + k'^2 - 2kk'\cos\theta)^{1/2}$. Therefore, $d\Omega$ can be replaced by $2\pi \sin\theta d\theta = 2\pi K dK / kk'$ and the $\left|\varepsilon_n(\vec{K})\right|^2$ can be written as $\left|\varepsilon_n(K)\right|^2$. Then the equation [2.25] becomes

$$d\sigma_n = \frac{8\pi m_e^2 e^4}{\hbar^4} \frac{1}{k^2} \frac{1}{K^3} \left|\varepsilon_n(K)\right|^2 dK \qquad [2.27].$$

The quantity $\varepsilon_n(K)$ is called the inelastic-scattering form factor, which is widely used in nuclear and particle physics. But a slightly different quantity, the generalized oscillator strength, introduced by Bethe [30] is more often used. In terms of Rydberg unit of energy $R = me^4/(2\hbar^2) = 13.606 eV$ and the Bohr radius $a_o = \hbar^2/(me^2) = 0.52918 \times 10^{-8} cm$, that is defined as

$$f_n(K) = \frac{E_n}{K^2 a_o^2 R} \left|\varepsilon_n(K)\right|^2 \qquad [2.28].$$

Let us consider the behavior of the generalized oscillator strength in the limit of vanishing K. For $K \to 0$, the exponential in equation [2.26] can be expanded in terms of K. For an optically allowed transition, the first order of K in the series will be dominant. By using the orthogonality of ψ_n and ψ_o, we get

21

$$\lim_{K \to 0} f_n(K) = \frac{E_n}{R} M_n^2 \qquad [2.29]$$

where $M_n^2 = \left| \int \psi_n^* \sum_{j=1}^{Z} x_j \psi_o d\vec{r_1} ... d\vec{r_Z} \right|^2 / a_o^2$ is the dipole matrix element squared, x_j

is a component of $\vec{r_j}$. The quantity on the right-hand side of the equation [2.29] is

known as the optical oscillator strength f_n, which defines the magnitude of

photo-absorption into the nth state of the target. Equation $\lim_{K \to 0} f_n(K) = f_n$ exhibits the

relation between the collision of fast electron and photoabsorption. In the case of

high-energy collision, most incident electrons are scattered forward or nearly forward,

and the momentum transfer is small. Thus, the generalized oscillator strength can be

replaced, to a good approximation, by the optical dipole oscillator strength in equation

[2.27]. The integral cross section for an optically allowed transition is obtained by

integration. It has been discussed in great detail by Inokuti [31]. In terms of

$E = (1/2)m_e v^2$ and f_n, the integral cross section is

$$\sigma_n = \frac{4\pi a_o^2 R^2 f_n}{EE_n} \ln(\frac{4C_n E}{R}) \qquad [2.30]$$

where C_n is given by

$$C_n = (\overline{K} a_o R / E_n)^2 \qquad [2.31]$$

in which $\overline{K}$ is the average momentum transfer for the collision. Equation [2.30]

indicates that the integral cross section for a dipole allowed transition decreases as

$\ln(E)/E$ for fast electron collision.

In the preceding section, it has been mentioned that we can obtain an

excitation function, which is viewed as relative cross section, in the experiment. One

of the advantages of the equation [2.30] is that it aids in obtaining absolute cross

22

section from relative data if the optical oscillator strength for the transition, f_n, is known. (Assume that all of the target particles on the state ψ_n are excited directly from the state ψ_o due to electron impact.). The calibration procedure involves Fano plot [32], which is a plot of the product of count rate and electron impact energy against the natural logarithm of the electron impact energy. At sufficiently high impact energies, Fano plot approaches the asymptotic behavior of straight line whose intercept on the energy axis is $E_{int} = R/4C_n$. By knowing f_n and obtaining C_n from Fano plot, the integral cross section can be calculated for high collision energy, from which the absolute cross section at the rest energy range can be evaluated.

Considering the optically forbidden transition, the dipole term in the expansion of exponential in the equation [2.26] vanishes, and the quadrupole term is dominant. At high impact energies, it is shown that the excitation function in such a case falls off with E^{-1} dependence. Optically forbidden states are often associated with excitation of metastable states.

So far, we have neglected influence of the exchange of the incident electron with the electrons in the target molecule. In the event that electron exchange occurs, Ochkur (1964) [33] showed that the exchange cross section decreases as E^{-3} at high impact energy. There is appreciable probability of electron exchange only when the velocities of the incident electrons are comparable with the velocities of the molecular electrons. As the incident electron energy increase, the probability becomes smaller and smaller, and then the excitation cross sections decrease rapidly.

Another method for calibration, which is related to this work, will be

23

introduced in following. If an integral cross section of the same metastable fragment released from another target gas is known, the excitation function can be put on an absolute scale by comparison under identical experiment conditions. Since this approach involves two target gases with different molecule weight, which have the different flow rate through the capillary, the relative target gas densities should be taken into account as a correction factor.

Let us go back to equation [2.21]. In practice, it is impossible that detector identifies all of metastble fragments arriving at the surface of detector. The detection efficiency, q, is defined as the ratio of particles counted by a detector to the actual number of particles incident on the detector. By considering the detection efficiency and the effect of the collisions between metastable fragments and the background gas, a little modification should be made to the equation [2.21]. Then the metastable fragment count rate, R_M, is given by

$$R_M = qe^{-N_x\sigma_x D}\sigma\frac{\Omega}{4\pi}\int N_e(x,y,z)v_e(x,y,z)N(x,y,z)dV \qquad [2.32].$$

where Ω is the solid angle subtended by the detector. The exponential factor, which is determined by Beer's law, shows that collisions with background gas make the metastable fragment beam decreases exponentially with flight length, D, the background gas number density, N_x, and the collision cross section between the metastable fragments and the background gas, σ_x.

It is well known that

$$I = N_e ev_e A \qquad\qquad\qquad\qquad [2.33].$$

In our case, I is the current of the electron beam measured by a faraday cup, e is

the electron charge, and A is the cross sectional area of the beam. By substituting

equation [2.33] into equation [2.32], we have

$$R_M = qe^{-N_x \sigma_x D} \sigma \frac{\Omega}{4\pi} \frac{I}{eA} NV \qquad [2.34]$$

where N represents the average number density over the collision volume V

formed by the intersection of the electron beam and gas jet.

Applying the equation [2.34] to a target gas with a known cross section for the

metastable fragment and to another target gas with a unknown cross section for the

same metastable fragment, we obtains the metastable fragment count rate R_m and

R_m' respectively. Dividing R_m' by R_m, the unknown cross section, σ', can be

expressed in terms of known cross section, σ, as

$$\sigma' = \sigma \frac{R_m' IN}{R_m I' N'} \qquad [2.35]$$

It is noted that assumption that the attenuation coefficient is approximately same for

both gases is used for derivation of equation [2.35].

If the "molecular flow" conditions that the mean free path of the target gas is

significantly greater than the inner diameter of the capillary tube ejecting the gas

beam, d, is satisfied, the number density of target gas is proportional to the source

pressure, and the spatial distribution of molecules within the beam is determined by

the geometry (the ratio l/d) of the capillary [34]. Then, the equation [2.35] transforms

into

$$\sigma' = \sigma \frac{R_m' IP}{R_m I' P'} \qquad [2.36]$$

(For the further discussion of the case of high source pressures, see LeClair (1993)[35]

25

or Trajmar and McConkey (1993)[36] and references therein.)

Systematic Errors

(a) Finite Electron Pulse Width

In TOF spectra, the arrival time t is respect with the center of the electron pulse that serves as time origin. However, the whole width of the electron pulse, Δt, contributes to the TOF distributions. If this contribution is taken into account, the TOF distributions are broadened and thereof the corresponding kinetic energy distributions are spread. This effect in RKE distribution is given by

$$\Delta T_{ER} = T_{ER} \cdot \frac{2\Delta t}{t} \qquad\qquad [2.37].$$

It is clear that the uncertainty of RKE distribution becomes serious at short flight times.

(b) Thermal Energy Spread of the Parent Molecules

If the parent molecules have thermal motion component along the detector axis, an extra contribution, either positive or negative, will be given to the velocity of the fragment. The uncertainty in fragment velocity can be translated to the kinetic energy. The resultant spread in RKE distribution due to thermal motion of target molecule is given by [37]

$$\Delta T_{ER} = 2\sqrt{2E_{th}T_{ER}} \qquad\qquad [2.38]$$

where E_{th} is the average thermal energy of the parent molecule. This uncertainty increases as RKE increases. In practice, we arranged the electron beam, target gas

26

beam, and the detector to orthogonalize each other in order to reduce the component of thermal motion along the detector axis.

(c) Uncertainty in the TOF distance

Like the effect of finite pulse width, the uncertainty in the flight distance causes the error in the RKE, especially at short flight time region. The mathematical expression for this effect is given by

$$\Delta T_{ER} = T_{ER} \cdot \frac{2\Delta D}{D}$$ [2.39].

The uncertainty, ΔD, may result from the diameters of electron beam and gas beam, the angle of acceptance, and spatial extent of detector. In our case, the D is 265mm. For the approximately 1mm wide electron beam and 1mm wide gas beam, the corresponding error in RKE is negligible. However, the surface of detector (channeltron) should be considered. The channeltron has a cone shape surface with approximately 10mm entrance diameter and 10mm depth. Since the main surface of acceptance is the vicinity to the entrance, the reasonable uncertainty ΔD is given by the half of the cone depth (5mm), which results in the error in the RKE of about 4%.

(d) In-Flight Decay

For a long flight distance, the metastable fragments with low kinetic energy, which corresponds to long flight time, may decay before they reach the detector and thus the RKE distribution is influenced at low energies. The correction for in-flight-decay has been developed by Mason and Newell [38]. This uncertainty can

27

be estimated when the lifetime of the metastable fragment is known. For our subjects H(2s) and O(^{5}S), the lifetimes are known as about 0.12s for H(2s) and about 180us for O(^{5}S). No direct evidence showed that this effect becomes significant.

(e) Recoil Effects

During the collision, the electrons transfer part of momentum to the parent molecule. However, for the relative heavy molecules, this influence is not significant. That has been shown by experiments and theoretics. As an example, the recoil effect in a 20eV electron impact to N_2 or heavier molecules leads to a RKE spread of 0.1eV [37]. For the target molecule in our experiment, this error is negligible.

(f) Timing and Sampling errors.

In this experiment, the TOF spectra are acquired by using a multi-channel scalar, which counts incident pulse signal in successive time bins. Each time bin has finite width. That may introduce significant errors in RKE distributions at high kinetic energy as the width of the electron beam pulse dose. In this work, the bin width was set to be 320ns, which is much shorter than width of the electron pulse. Compared with the effect of width of electron pulse, error due to width of time bin is negligible.

(g) Detection efficiency versus metastable fragment velocity.

In present work, a channeltron (channel electron multiplier) is expected to be employed to probe the neutral metastable fragments produced in electron impact.

28

Malone [39] has shown that there appears to be only a little change in detection efficiency with the speed of input fragments.

(h) Angular distribution of the fragment.

During the electron impact dissociation, the excitation probability in dependence on the relative orientation of the excitation of the exciting beam and some axis of the molecule can cause the products corresponding angular distribution. Anisotropies in such distribution only become significant with relatively simple molecule like H_2, and low impact energies near threshold [35]. As impact energy increase, the angular distribution tends to be isotropic rapidly (eg. Misakian et al, [40] for work on CO_2). In our situation, fragments are assumed to fly apart identically in all directions.

Chapter 3

Experimental Details

The Vacuum System

Figure 3.1 gives a schematic diagram of the entire apparatus, each aspect of which will be described in detail in the following text.

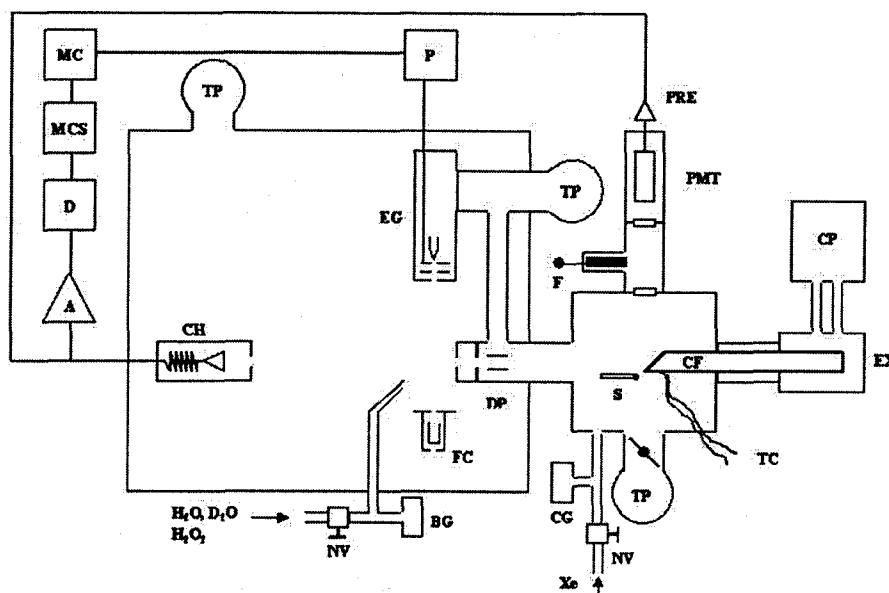**Figure 3.1.** Schematic diagram of the apparatus. A-pulse amplifier; D-discriminator; P-pulser; F-filter; TP-turbo pump; EG-electron gun; FC-Faraday cup; BG-Baratron gauge; NV-needle valve; DP-deflection plates; CG-convectron gauge; CF-cold finger; TC-thermocouple; PMT-photomultiplier tube; MCS-Multichannel Scaler/Averager; MC-master clock; PRE-preamplifier; S-shutter; CH-Channeltron detector; EX-Expander; CP-compressor.

The system consisted of four differentially pumped chambers that are connected with O-rings. The lowest pressure of the system could reach 2×10^{-7} torr. A 1000 l/s turbo pump (TP) (Varian model TV-701) was utilized to evacuate the main chamber (The large cube shaped chamber), and the pressure measurements were obtained by an MKS 941 cold cathode gauge. Electron gun (EG), target gas jet, and channeltron detector (CH) were mounted in this main chamber. A detector chamber housing the cold finger (CF) was connected to the main chamber through a port on right side of the main chamber. Channeltron detector and the cold finger were arranged in the same axis. The electron beam, gas jet, and the axis of detectors were mutually orthogonal.

Electron gun chamber which housed the electron gun was kind of T shaped chamber. Electrical circuit was connected to the electron gun through a ceramic feedthrough on the rear flange of the chamber. On the bottom of the electron gun chamber, there was a 4 cm diameter pipe through which the chamber was differentially pumped by a second 1000 l/s turbo pump (Varian model TV-701). Experience of preliminary work [41] taught us that this kind of differentially pumping design, which could reduce corrosive action of O_2 on the hot filament, and increase the lifetime of the filament, was necessary. The next section will give the further details about the electron gun.

Detector chamber consisted of two parts, deflection plate chamber and cold finger chamber. Deflection plates (DP) separated by 1 cm was set in a small chamber, $3 \times 2.5 \times 2.5$ cm in size, which was evacuated by the same turbo pump used for the

31

electron gun chamber through a 4 cm diameter tube. The function of the defection plates was to remove ions and electrons and to quench Rydberg species. The entrance of the deflection plate chamber, an aperture 2.5 mm in diameter, was located 2.2 cm away from the collision region. Another aperture with the same diameter was set 2.5 cm from the entrance in the chamber. Both apertures were blackened with soot to reduce the amount of filament light reaching the photomultiplier. After the deflection plates, the third blackened aperture with a diameter of 8 mm is located 7.3 cm from the axis of the electron beam. The cold finger chamber was pumped through the deflection plate chamber. Therefore, the third aperture could be used to limit the pumping speed and to reduce the consumption of xenon. Products of dissociation passed through all three apertures to reach cold finger.

In the cold finger chamber, xenon gas deposited on the surface of cold finger to form a solid layer under a low temperature. The surface had an angle of 45 degree with respect to the flight path. The flight path length, D, which was defined from the interaction region to the center of surface of the cold finger, was 26.6±1.0 cm. A gate valve (not shown in the figure) was installed between the defection plates and the cold finger. When the filament needed to be replaced, the gate valve was closed to isolate the cold finger chamber. The pressure of the cold finger chamber was maintained by a small 200 l/s turbo pump (Sargent Welch 3134). In normal case, a butterfly valve was shut down to separate the small turbo pump and the cold finger chamber. In preliminary work, this design was used to avoid the exposure of the detector chamber to the atmosphere to keep cold finger clean. A small window was set on the chamber,

32

which was convenient to us to watch the xenon layer on the cold finger.

Both turbo pumps were backed with a large rotary vane rough pump (Varian DS 1002 3Ph). The detector chamber turbo pump was backed by a small rotary vane pump (Edwars ED100). The foreline pressure of rotary pumps was measured by convectron gauges, which are controlled by appropriate convectron gauge controllers (Grannille-Phillips 316). Normally the foreline pressure was approximately 15 mtorr. Unfortunately, we did not have safety interlock in the control circuit to protect turbo pumps in case of failure of the forepumps. Our vacuum was very clean and oil free, which was necessary to avoid contamination of the cold finger caused by oil vapors.

The electron gun and gas jet

Figure 3.2 shows a scale diagram of electron gun, and Figure 3.3 shows the electrical connection. The basic idea of the electron gun came from design of Ajello et al. [42], but the original design was simplified. The electron consisted of two electrodes and a filament.

A 0.75 mm wide iridium ribbon filament was welded on the filament holder and carefully aligned with the slit, 1.0×5.0 mm in size, on the extraction electrode (EE) in order to reduce the effect of scattering and secondary emission from the edge of the slit. It usually needed 5 to 6 amps of current to produce a usable beam. The extraction electrode was utilized as positive anode, which received a pulse to extract the electrons emitted by filament. The whole electron gun was set along the axis of a permanent magnet quadrupole to collimate the electron beam. Electrons in the beam

33

were kept from diverging due to the mutual electrostatic repulsion by the Lorentz force. Every component of the gun and Faraday cup, except for the molybdenum slit on the collimation electrode (CE), was made of non-magnetic stainless steel.

A double faraday cup was mounted 4.5 cm far away from the filament to monitor electrons. Two cups were electrical isolated each other. The inner faraday cup, 9.4mm diameter and 11mm length, had an applied bias with respect to ground. All of the current (99.99%) was intercepted by inner cup and the typical current was 1mA d.c. in the absence of a gas jet. [43]. A plot of beam current versus beam energy is shown in Figure 3.4, which was obtained by LeClair [43].
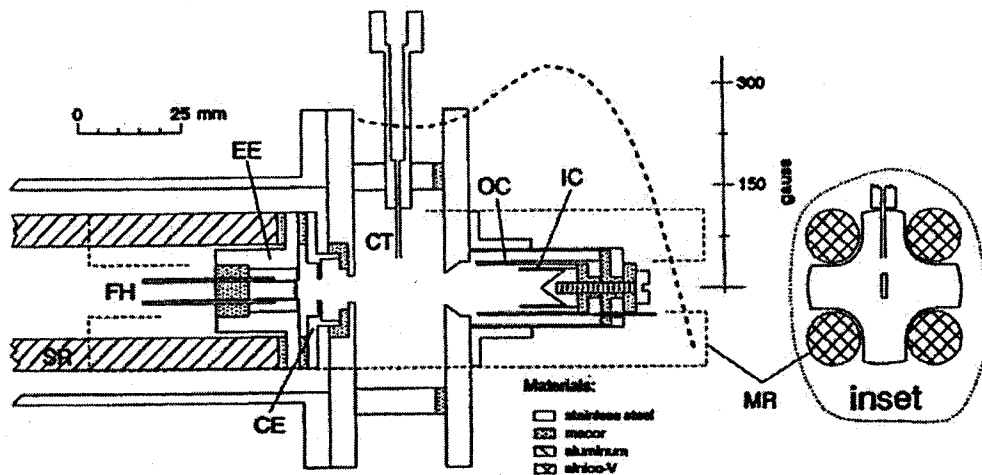
Figure 3.2. Profiles of the electron gun, faraday cup, and gas jet. SR-support rods; FH-filament holder; EE-extraction electrode; CE-collimation electrode; CT-capillary tube; IC-inner cup; OC-outer cup; MR-magnetic rod. The positions of the magnetic rods are partially drawn in with a light dashed line. The inset shows the orientation of the magnet rods to the electrodes, and the slits to the gas jet. The heavy dashed line represents the magnitude of the magnetic field along the electron beam axis, according to the scale at right.

34
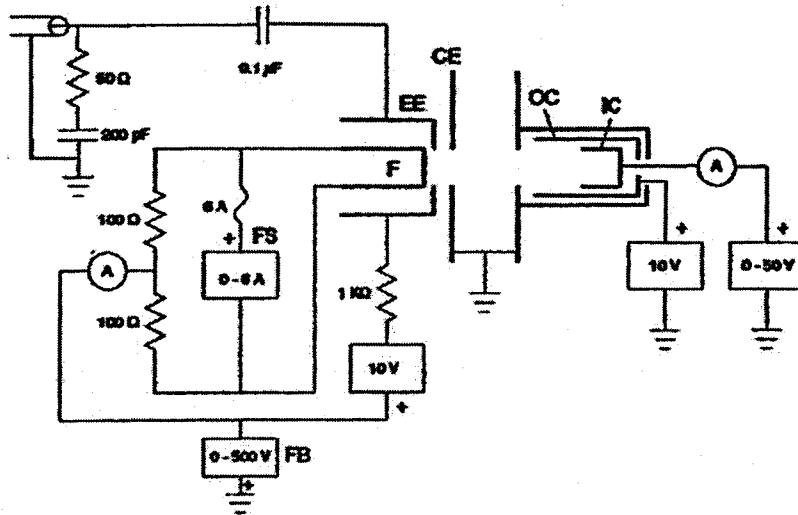
Figure 3.3. Wiring diagram for the electron gun operating in the pulsed mode. F-filament; EE-extraction electrode; CE-collimation electrode; OC-outer cup; IC-inner cup; FS-filament supply; FB-filament bias supply which determines the energy of electrons (E_0) along the axis at the interaction region.

Figure 3.4. A plot of current entering the inner faraday cup versus electron impact energy using O_2 as the target gas (10 torr upstream of the nozzle). The inner faraday cup was biased at +50V, the outer cup at +10V. Pulses were 20us long at a rate of 5.0KHz.

35

Figure 3.3 describes the electrical circuit of the electron gun. Stable and accurate power supplies were used to provide voltages an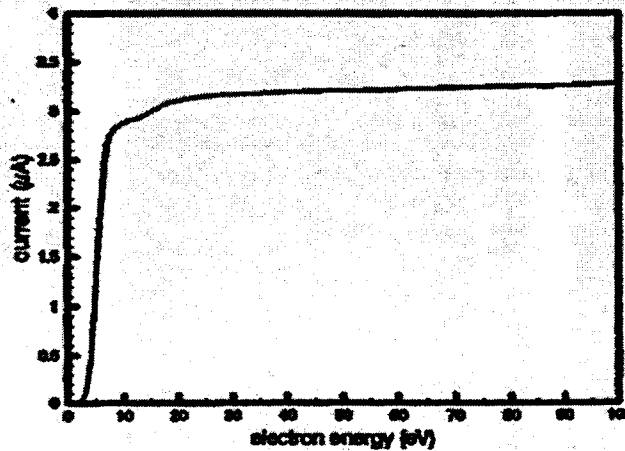d to define the electron beam energy. When a +35 V pulse was applied on the extraction electrode, which had -10V bias with respect to the filament, through a 0.1 uF capacitor, the electron gun produced pulse of electron (2.5 to 70 us long). The coaxial cable was grounded through a 50 Ω resistor and 200 pF capacitor. In this way, the reflection of high frequency component was reduced. Change of the extraction pulse height leaded to the change of beam currents. The pulse currents entering the inner cup were measured by a digital ammeter with an integrating input function. The current measurements had a relative accuracy of 0.5%.

In this design of electron gun, a magnetic field was introduced to collimate the electron beam. The magnetic field was supplied by the magnet quadrupole composed of four 15 cm long Alnico-V magnetic rods with a diameter of 1.25 cm. The axes of the electron gun and Faraday cups coincided with the axis of symmetry of magnetic field. The measurement of the magnetic field had been done by LeClair [43]. A plot of the magnetic field along the axis is also shown in Figure 3.2. According to LeClair, magnetic field off axis had small deviations of about 5% at a distance of several millimeters.

The amount of the filament bias determined the beam energy at the interaction region, E_o. Several factors were considered to affect that E_o. During the operation, it was assumed that every part of the filament had the same electrical potential.

However, in reality, there were about 2V voltage across the filament. Spread of bias on the surface of filament resulted in a distribution of electron energy. Another influence of the spread of energy was thermoionic emission. This Maxwellian type distribution was typically about 2eV for a filament at 2320K [44]. The bias on the inner faraday cup also produced significant field penetration extending into the interaction region. This effect brought on a several volts change of the average beam energy when the voltage on inner cup was +50V [43]. One further influence was the depression of the potential at the interaction region caused by the repulsive interaction of electrons, which resulted in the several volts threshold shift when a too high beam current was used. In the following part, we will discuss the beam energy calibration for threshold.

Gas beam was introduced through a capillary tube (CT) with an internal diameter of 0.66 mm. The axis of the capillary tube located 2.5 cm away from the filament was perpendicular to the coincident axis of electron gun and faraday cups, and the distance from the orifice to the electron beam axis was 7.5 mm. An MKS Baratron gauge (BG) was used to provide the measurement of source pressure upstream of the capillary, P. The pressure of main chamber reduced to the order 10^{-4} torr, when P was about 10 torr, a typical operation pressure.

Detectors

When the temperature was low enough, the xenon gas frosted over, and the solid layer of xenon grew on the surface of the cold finger, which was cooled down by

37

a closed cycle cryogenic refrigerator. The cold finger, whose tip was polished to a mirror finish, was mounted on the second stage heat station of the refrigerator with good thermal conductivity. The whole cooling system is shown in Figure 3.5. The refrigerator consisted of expender (DE-202AF) and compressor (ARS-4HW). The expender, which provided two levels of refrigeration (the first stage and second stage heat stations), was mounted in the cold finger chamber. The first stage and second stage heat stations exposed to vacuum. The compressor was connected to expander by two gas lines. It operated on the principle of the Giffor-McMahon refrigeration cycle. The high pressure helium gas flowed into the expander, then the gas was vented to the low pressure and returned back to the compressor. Meanwhile, the low pressure gas brought the heat out of the expander. The second stage heat station got cold. The minimum temperature could reach about 9K. The gas was compressed by compressor, and started another cycle. Compressor could supply pressure by 270±20 psi (gauge) during the operation. Cooling water was needed to maintain compressor's operation.

Two silicon diode sensors (LakeShore DT-670) were utilized to measure temperature. One was fixed near the tip as a sample sensor; the other one was fixed on the second stage heat station as a control sensor. Sensors sent the voltage data back to temperature controller (LakeShore 331E), which translated sensor inputs into temperatures by using temperature responding curve and sent out control signal to the heater (36Ω) on the second stage heat station to keep cold finger at exactly the setpoint temperature we entered. The heater output could supply up to 50 W of continuous power to a resistive heater. (The maximum current is 1A and maximum

38

compliance voltage is 50V.)

Xenon was ejected into cold finger chamber through needle valve. The xenon pressure out of needle valve was probed by a Granville-Phillips Convectron gauge (CG in Figure 3.1).
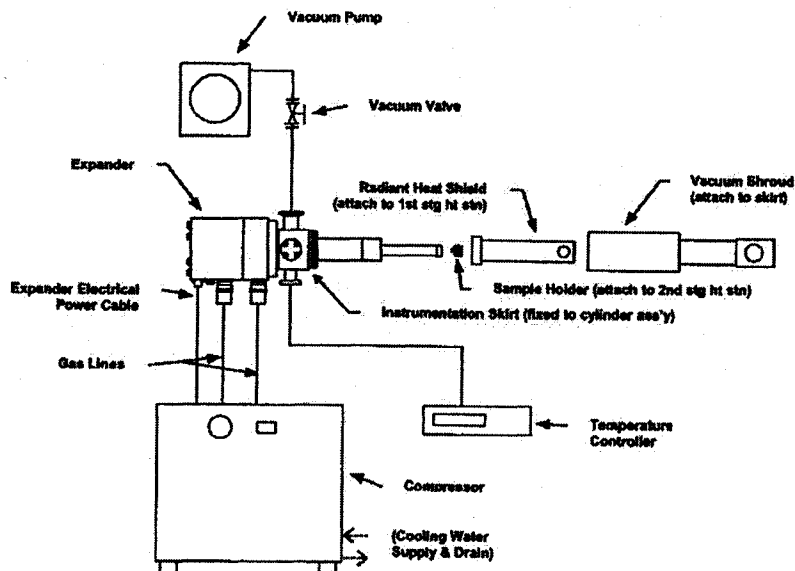

Figure 3.5. The diagram of the cooling system, from the manufacturer.

Metastable $O(^1S)$ atoms reaching the solid xenon quickly formed a weakly bound molecule with Xe in an excited energy state but not in their ground state. Such molecules are called excimers. Excimers rapidly emitted fluorescence corresponding to the transitions between excimer states. A cooled photo-multiplier tube (PMT, Hamamatsu R943-02) was placed 23.6 cm away from the xenon surface to detect the photons. The angle between the axis of photo-multiplier tube and the normal of the cold finger surface was 45 degree, and the axis of photo-multiplier tube was

39

perpendicular to the axis of the cold finger. The PMT in a magnetic shield was

coupled to socket assembly (Hamamatsu E2762). The whole assembly was clamped

in the cooling unit (Hamamatsu C4877). The minimum temperature could be -30°C

with room and cooling water temperatures of $+20^\circ$C. In our work, we used this

minimum temperature. Dark counts were about 4 counts per second at -30°C. Figure

3.6 shows the plot of quantum efficiency versus wavelength. The PMT was operated

at a bias of about 1800V.

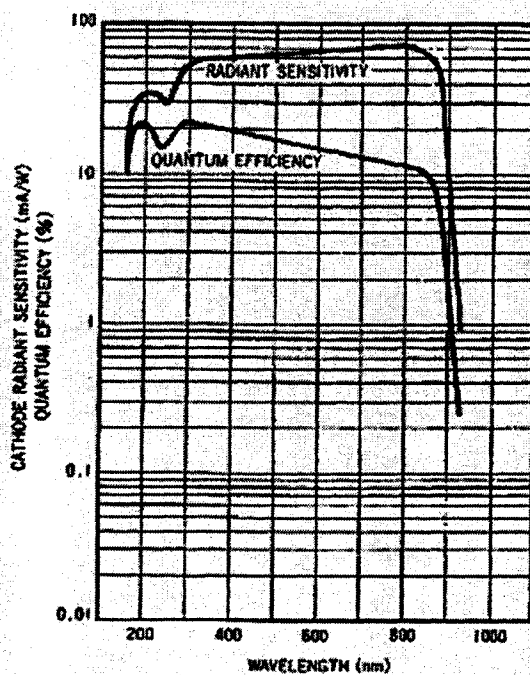**Figure 3.6.** Quantum efficiency of the GaAs (Cs) photocathode of the Hamamatsu R943-02 photomultiplier tube, from the manufacturer.

The scheme of $O(^1S)$ detection discussed above adopted the emissions in the

Xe layer deposited on the cold finger. Therefore, the quality and the thickness of the

Xe layer, which obviously depend on the cold finger temperature and the Xe vapor

pressure, could be important factors affecting detection efficiency. Moreover, high Xe

vapor pressure might cause high probability of collision between Xe and $O(^1S)$ so that

count rate decreased. Figure 3.7 and Figure 3.8 illustrate the pressure dependence and

temperature dependence of detection efficiency when the CO_2 was taken as target at

impact electron energy of 100eV. The y coordinate in the diagram represent the ratio

of $O(^1S)$ yield to prompt photon yield. These two kinds of dependence had been

measured by LeClair [43]. Our pressure dependence was close to the result of LeClair.

In LeClair work, he only reported the temperature dependence in the range from 70K

to 80K. Since the cryogenic refrigerator, rather than liquid nitrogen, was used to cool

cold finger in present work, the lowest temperature limit of the temperature
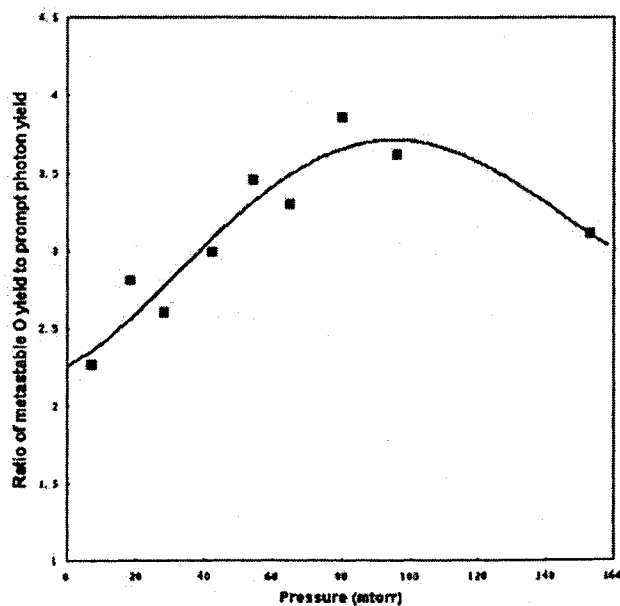
dependence was extended up to 9K.

Figure 3.7. Ratio of $O(^1S)$ yield to prompt photon yield versus Xe pressure. CO_2 was used as the target for $O(^1S)$ production.

41
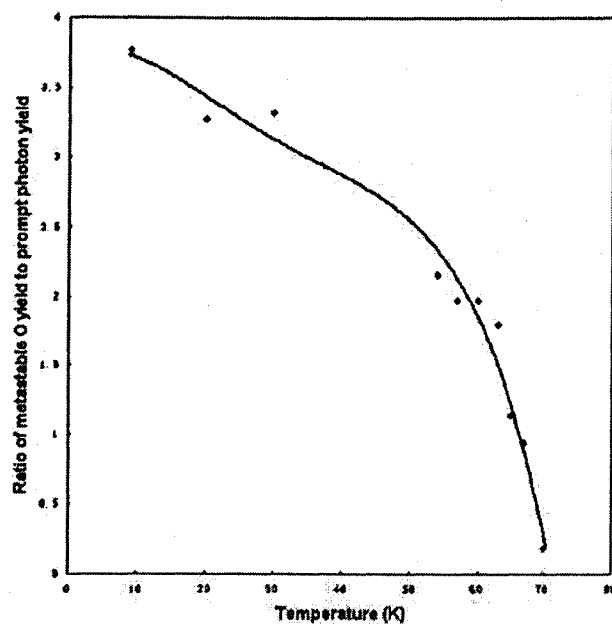
Figure 3.8. Ratio of O(^{1}S) yield to prompt photon yield versus cold finger temperature. CO_2 was used as the target for O(^{1}S) production.

As shown in Figure 3.1, a channeltron (Burle/Galileo 4039) was located at a distance of 27 cm from the interaction region in the main chamber. In order to block unwanted ions and electrons and quench Reydberg species, two grids separated by 2 mm were placed vertically in front of the channeltron's cone. The grid on the interaction region side was grounded to keep the same potential as the interaction region. When an excited atom approached the surface of the channeltron it was energetically possible that the atom returned to ground state and the energy was transferred to an electron in the surface. If the excitation energy of the atom exceeds the work function the electron will escape from the surface. The electrons ejected

42

from the surface multiply due to secondary emission in the channeltron and eventually formed an out signal. According to previous work [45], the upper wavelength cut-off of the channeltron was around 150 nm. That meant that the minimum energy required to liberate surface electron was about 8.3 eV. Therefore, this allowed us to probe $O(^5S)$ (excitation energy of 9.15 eV) and H(2s) (10.2 eV) by using channeltron. Because the excitation energy of $O(^1S)$ (4.19eV) is lower than 8.3 eV, the channeltron will blind to $O(^1S)$. 3 KV bias was applied on the channeltron.

During the operation, a sudden drop on tail of the prompt photon peak was observed when the counts per second were very high. The key factor of affecting the maximum count rate capability is the bias current, which supplies electrons to maintain the secondary electrons emission. High count rate leads to high secondary electrons emission rate. When the count rate increases and the output current approaches the bias current, the gain begin to decrease because of lack of electrons. Eventually, the pulse amplitudes are lower than the level of the discriminator, which could cause a sudden drop in the signal output ("dead time"). The prompt photon peak was the highest peak in the TOF spectra. The highest count rate occurred during that peak. Therefore, such sudden drop was most likely to happen to the prompt photon peak when count rate was fast. Figure 3.9 shows how the count rate affects the shape of prompt photon peak. This figure was acquired at 100eV electron impact energy by using H_2 as target. It is clear that when the count rate is below 100 counts per second, the sudden change becomes unconspicuous on the shape of prompt photon peak. Therefore, the maximum count rate is about 100 counts/s. The maximum count rate

43

can also be expressed with the respect to the unit of counts per pulse. Since our electron pulse has period of 1000us, the maximum count rate (100 counts/s) should be 0.1 counts/pulse.
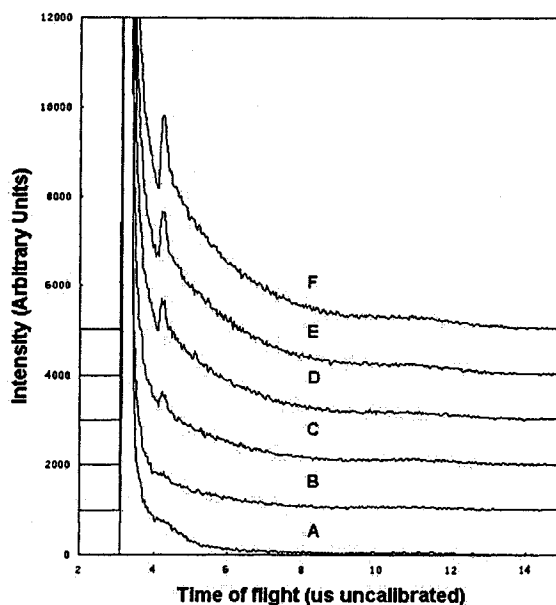
Figure 3.9. TOF spectra of electron impact dissociation of H_2 at 100eV. The count rates are: A: 50 counts/s (0.05 counts/pulse); B: 100 counts/s (0.1 counts/pulse); C: 150 counts/s (0.15 counts/pulse); D: 200 counts/s (0.2 counts/pulse); E: 250 counts/s (0.25 counts/pulse); F: 300 counts/s (0.3 counts/pulse).

Data Acquisition

Standard nuclear instrumentation modules (NIMs) were involved to process signals from the detectors. The data acquisition scheme is included in the Figure 3.1. When the photomultiplier was used, pulses were first amplified by a homemade pre-amplifier with 10 times gain and then fed into a timing filter amplifier (Ortec 454) which was set at a gain of 50. In case of channeltron, pulses were directly furnished to

44

amplifier. A discriminator followed the amplifier. When the input exceeded an appropriate threshold level, an output signal was sent to a multichannel scaler (MCS, SR430) that was used to obtain TOF spectra. A counter was also connected to discriminator output to monitor count rate.

The MCS counted incoming pulses in successive time bins (channels). 1k time bins with the same time interval of 320ns for each bin were set. A trigger activated a sweep over all time bins. During each time bin, incoming pulses were counted. There was no dead time between time bins and no pulses were missed at the bin boundaries. If repetitive trigger was applied on the MCS, counts of the same time bin for each sweep were accumulated. Thus, a list of counter data corresponded to a distribution of pulses over time. The data were stored in a floppy disk. Accumulation only occurred after one sweep was complete. That resulted in an accumulation dead time (250ns per bin and a fixed overhead 150us). The total accumulation capacity of each time bin was 32,767, and the maximum count rate was 100 MHz. An insertion delay from trigger to the first bin was 45 ns, and the signal counted by MCS was delayed by 20 ns. Therefore, all pulses that were 25 ns after trigger were captured in one sweep.

The timing of the system was controlled by a master clock (MC) that was a homemade unit with three delayed outputs. One of these outputs was used to trigger an electron gun pulser (P), and the other one was used to trigger MCS. The homemade electron gun pulser could generate 2.5 to 70 us pulses to fire electron gun. The electron pulse was delayed by 5 us relative to the trigger for MCS. This arrangement made MCS ready receive the prompt photons with very short flight times

45

which were generated due to electron impact excitation of target molecule in interaction region when the electron gun was fired. In practice, the prompt photons were treated as the relative zero of the time scale in TOF spectra.

The excitation function was obtained by a duel channel photon counter (SR400) that accumulated the counts in special time windows with respect to different electron impact energy. In excitation function case, the delayed output of the master clock that had been used for MCS provided the trigger signal for SR400. The SR400 output entered controller of the power supply for filament bias to produce step-changing voltage applying on the filament. The pulses from amplifier were fed into SR400 instead in this time. A computer was used to control the SR400 using a special program written in BASIC language. The control information like time windows, range of voltage change and number of sweeps was put into computer to start counting. There were 100 voltage steps between the low level and the high level set by program in each sweep. Accumulated data were saved to floppy disk after each sweep.

Chapter 4

H_2O and D_2O Results

Time-of-Flight Data

The series of Time-of-flight distributions for H_2O and D_2O obtained at various incident electron energies are shown on the following pages. Each spectrum was acquired during the same length of time using a 2.5 microseconds pulsed electron beam with a period of 1000 microseconds. The head pressure of the target vapor was approximately 2.5 torr, and the pulsed electron current was kept about 0.3 uA. The huge common peaks at short time are due to the prompt photons that reach the detector directly from the interaction region during the exciting electron pulse. The centers of these peaks are considered as the zero of time scale. A long tail following the photon peak expends towards the metastable signal for many microseconds. Since the prompt photons are the consequence of the fluorescence decay of target molecules or the fragments excited by electron impact, the tailing edge of the photon peak is related to the lifetime of those excited molecules or fragments. The number of particles on a excited state with lifetime τ is proportional to $\exp(-t/\tau)$. Although the structure of the photon peak is complicated, for a rough approximation, it is reasonable to assume that the intensity of the tail decreases with an exponential dependence on time.

47

Figure 4.1 Time of flight spectra for the fragmentation of H_2O produced by EID at the impact energies labeled.

48

Figure 4.2 Time of flight spectra for fragmentation of H_2O with long flight time on a magnified scale.
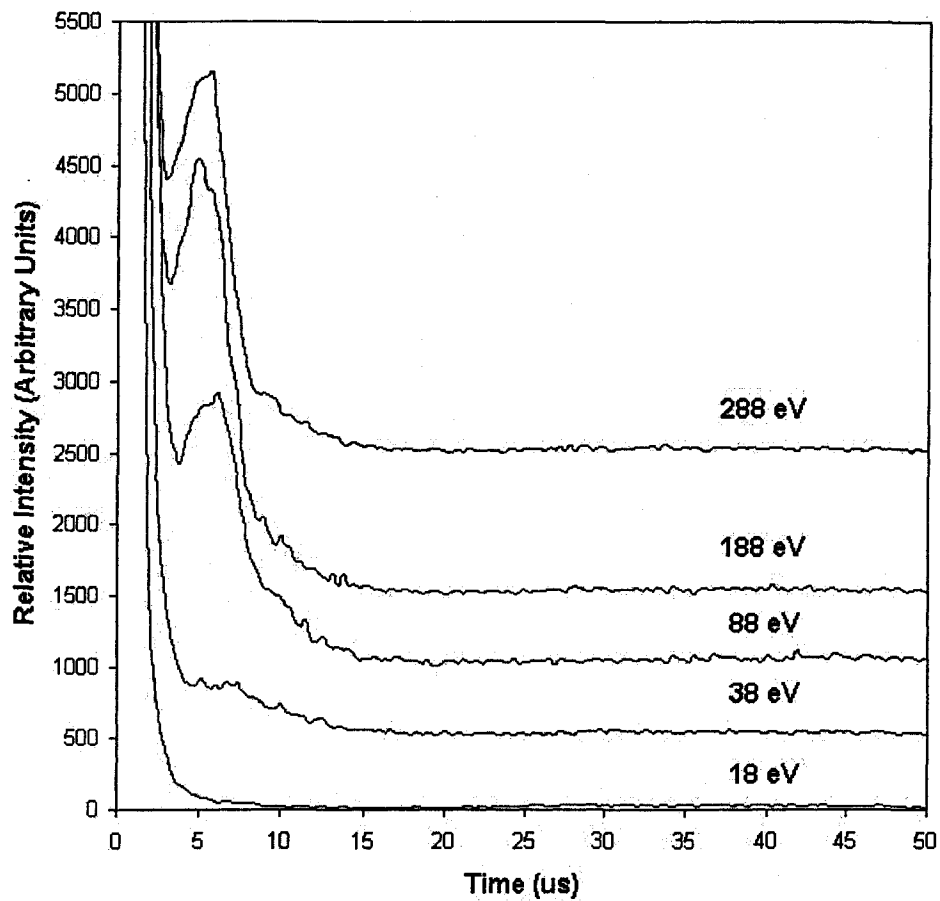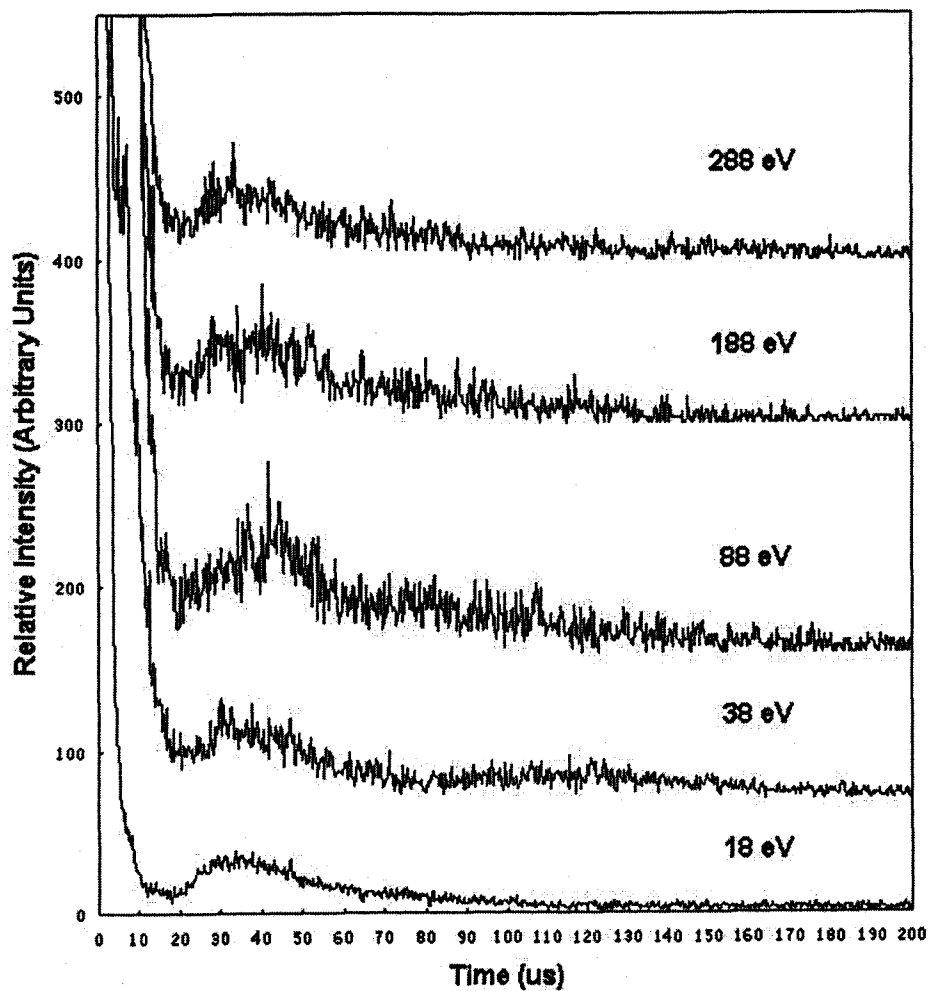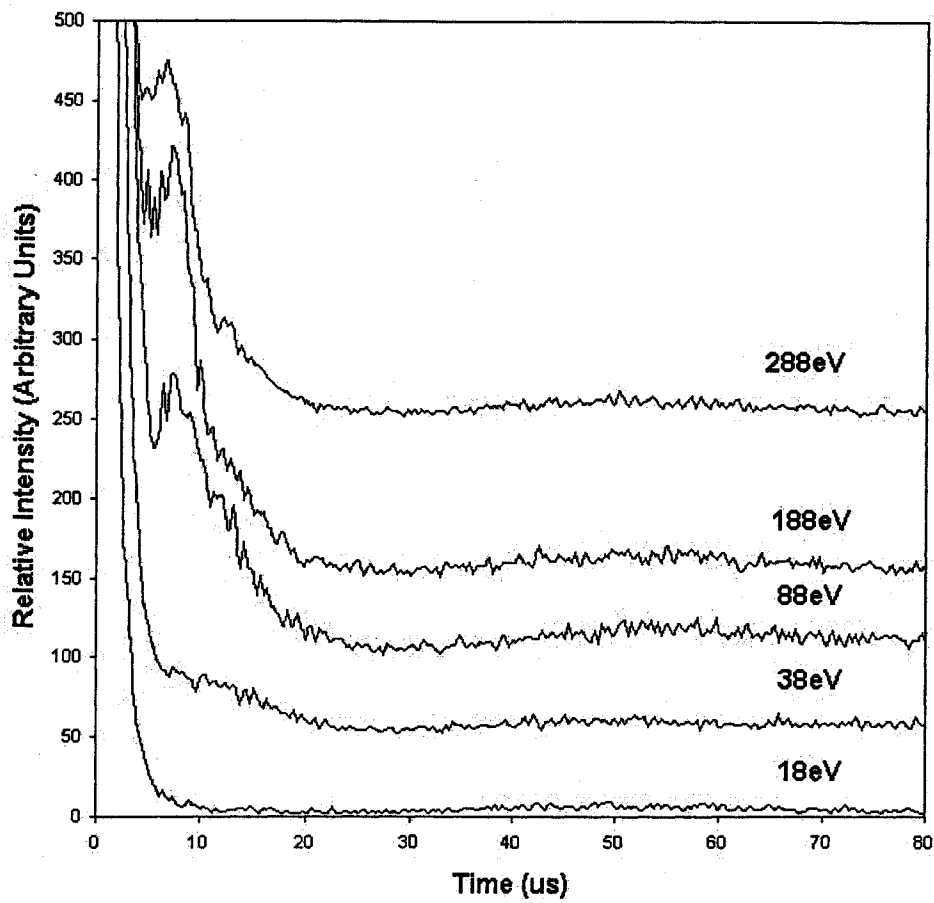
49

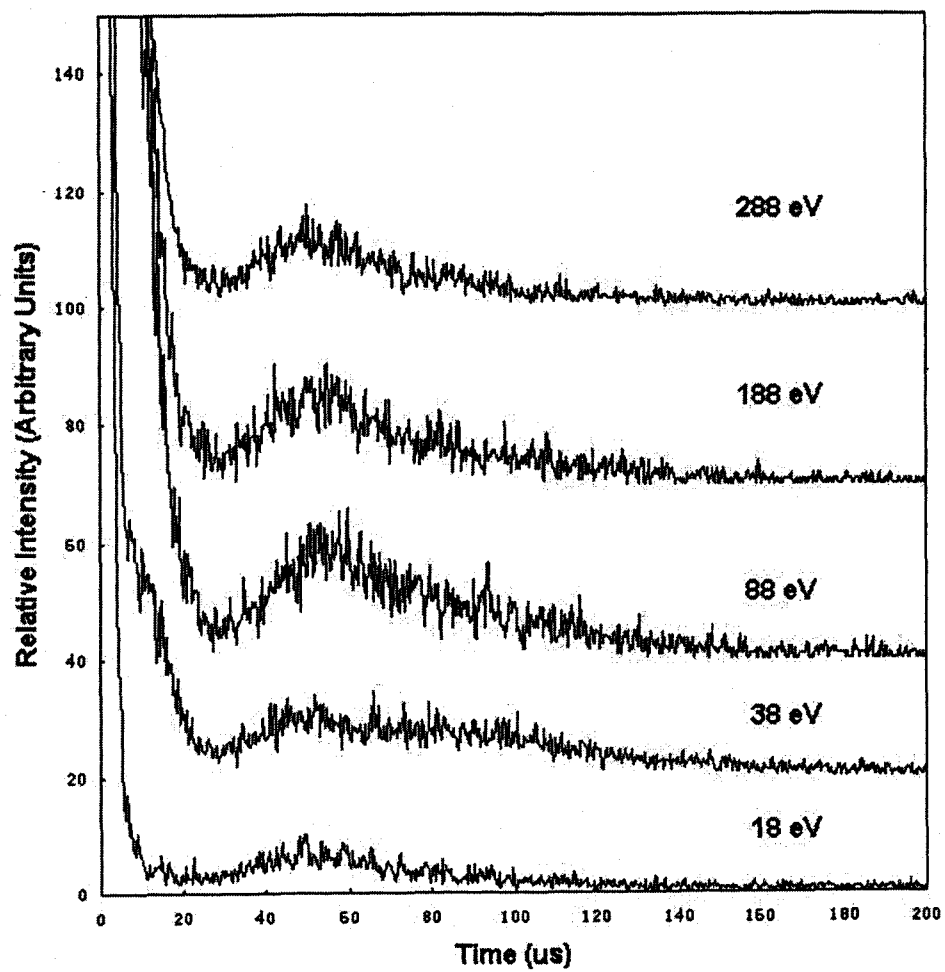**Figure 4.3** Time of flight spectra for the fragmentation of D_2O produced by EID at the impact energies labeled.

50

Figure 4.4 Time of flight spectra for fragmentation of D_2O with long flight time on a magnified scale.

51

TOF spectra obtained by using H_2O and D_2O as the target gases over the short flight times range are shown in Figure 4.1 and Figure 4.3, respectively, at several electron impact energies. The details of the structures at relative long flight times in TOF spectra of H_2O (Figure 4.1) and D_2O (Figure 4.3) are shown in Figure 4.2 and Figure 4.4 on the magnified scale, respectively. The TOF spectra have been shifted upwards, except for the 18eV curve.

The primary feature observed above 38eV electron impact energies in Figure 4.1 is clearly evident as a peak at approximately 5.5 us. This structure is barely observable at the impact energy of 18eV, and is observed as a shoulder at the impact energy of 38eV. It is clear that the relative height of this feature changes with increase of electron impact energy, and Figure 4.1 illustrates that it has the largest intensity when the impact energy is 188eV. As electron impact energy increases, the peak is observed to shift slightly to shorter times and it does not appear to broaden.

Figure 4.2 shows a magnified view of several tiny structures on the long TOF side of the primary peak. A broad slight peak spanning from 20us to 65us is observed to be maximized at approximately 35us. The intensity of this broad peak varies and its maximum shifts to the longer flight times as the electron impact energy increases. This structure manifests itself more clearly at electron impact energies around 88eV. There is no obvious broadening of this feature observed at different energies. Additionally, a new structure becomes more apparent as a shoulder on the long time side of the broad peak at impact energies greater than 38eV. The shoulder is observed to shift to shorter times (in other words, the broad peak and the shoulder move toward each other) with increasing electron impact energy. The possible reason for this shift is that more than one production channel are contributing to the broad peak (or the shoulder). Therefore, each feature (broad peak or shoulder) is a combination of

52

several TOF signals, each of which corresponds to one dissociation process. At different impact energy, the different process provides dominant contribution and thereby the distribution of intensities of the TOF signals corresponding to these channels varies with impact energy. As a consequence, the shape of the TOF spectrum is deformed when impact energy changes and it appears like a shift of the broad peak (or shoulder) along the time scale.

The structures seen in H_2O TOF spectra also exist in the D_2O TOF spectra, but they appear at somewhat different flight times. This interesting difference will be discussed later. A very fast fragment peaked at flight-time around 7us is shown in Figure 4.3. Figure 4.4 illustrates a broad tiny peak near 38us and a slight shoulder right behind the tiny peak. These features and their counterparts in H_2O TOF spectra vary in a similar way with electron impact energy.

The differences between the TOF spectra from the H_2O and the D_2O can be attributed to isotope effects. Although the same repulsive surfaces lead to identical corresponding total released kinetic energy for two isotopic molecules, the distribution of kinetic energy between fragments is different for the same dissociation process of the two isotopic molecules because of the different masses of the two isotopic fragments. The isotopic shift of TOF data is helpful to identify the fragment that is detected.

First, let us consider the situation of dissociation into two fragments. By using equation [2.1], equation [2.5], and $RKE(H_2O) = RKE(D_2O)$, it is easy to see that

$$(\frac{t(H_2O)}{t(D_2O)})^2 = \frac{m(H_2O)M_{H_2O}m'(D_2O)}{m(D_2O)M_{D_2O}m'(H_2O)} \qquad [4.1]$$

where labels 'D_2O' and 'H_2O' represent the dissociation process of heavy water and water respectively, t is the flight time of the detected fragment, m is the mass of the

53

detected fragment, m' is the mass of the undetected fragment, M is the total mass of the parent molecule (D_2O or H_2O). By applying equation [4.1] to all possible dissociation processes, we can draw some interesting conclusions. If the detected fragment is an oxygen containing species, equation [4.1] is greater than one. That is, the TOF peak for the fragment from D_2O shifts to shorter times relative to the same peak from H_2O. If a relative light fragment (H^* or D^*, H_2^* or D_2^*, or their ions) is detected, the equation [4.1] is less than one and thereby the peak for deuterium containing product shifts to longer times. Theoretically, equation [4.1] can be adopted for all possible kinds of two-body dissociations. For different kinds of fragments, the isotopic TOF ratio ($t(H_2O)/t(D_2O)$) has different values and therefore the detected fragment can be determined by measuring the isotopic shift. In practice, the values of these isotopic TOF ratios for different kinds of fragments are so close that it is unlikely to distinguish one from another due to experimental uncertainty, e.g. $t_{H_2^*}/t_{D_2^*} \approx 0.671$ and $t_{H^*}/t_{D^*} \approx 0.69$.

In the case of symmetric three-body breakup ($H_2O(D_2O) \rightarrow H(D) + H(D) + O$), the same derivation involving equation [2.10] and equation [2.11], as used in two-body situation, leads to the ratios of TOFs of hydrogen products and oxygen products from dissociation of H_2O and D_2O, which are written as

$$\frac{t_O(H_2O)^2}{t_O(D_2O)^2} = \frac{1 + \dfrac{8}{\cos^2 \alpha_{H_2O}}}{1 + \dfrac{4}{\cos^2 \alpha_{D_2O}}} \qquad [4.2]$$

$$\frac{t_H^2}{t_D^2} = \frac{1}{4} \cdot \frac{\cos^2 \alpha_{H_2O} + 8}{\cos^2 \alpha_{D_2O} + 4} \qquad [4.3]$$

where labels 'D_2O' and 'H_2O' represent the dissociation processes of heavy water and

54

water, respectively. If we substitute the average of $\cos^2 \alpha$ over the range from 0 to $\pi/2$, that is ½, for the term $\cos^2 \alpha$, equation [4.2] and equation [4.3] can be calculated. The results are $t_{O^*}(H_2O)/t_{O^*}(D_2O) \approx 1.291$ and $t_{H^*}/t_{D^*} \approx 0.687$, which means that the peak corresponding to the oxygen atom product from D_2O shifts to shorter times and the peak corresponding to the deuterium product shifts to longer times. Furthermore, it is clear that the value of t_{H^*}/t_{D^*} is very close to the value of the same TOF ratio for the situation of two-body dissociation, which makes it impossible to tell whether the process is two-body breakup or three-body breakup by measuring the isotopic shift.

By comparing the TOF spectra for H_2O and D_2O produced by 100eV impact electron beam, the difference manifests itself clearly, as shown in Figure 4.5 and Figure 4.6. The spectra have been scaled suitably so that the height of TOF peaks for H_2O and D_2O matches each other. Figure 4.5 shows the time shift between the primary features of the two targets. While the major peak for H_2O occurs at about 5.28us, the major peak for D_2O is observed near 6.56us. In other words, peak for D_2O moves to longer flight times relative to peak for H_2O. These two peaks are assumed to correspond to fragments from the same kind of dissociation process of H_2O and D_2O. According to the preceding discussion, the metastable fragments (or ionic fragment), which only contain hydrogen atom (or molecule), are responsible for the peaks that are slowed down by deuterium substitution (isotopic effect). There is a further proof that the primary peak cannot be due to an oxygen-containing fragment. It is noticed that this peak reaches the maximum at about 5.28us in the 100eV water dissociation TOF data. If the observed fragment were O* or OH*, the kinetic energies corresponding to the peak would be about 211eV or 224eV, respectively. Since the parent molecule is broken up by 100eV impact electrons, an oxygen-containing

55

fragment is clearly impossible.

In Figure 4.6, a magnified view of the structures at relative long flight times in 100eV H_2O TOF spectrum and 100eV D_2O TOF spectrum are shown. As the first sight was set on these tiny structures at long flight times in H_2O TOF data, it was guessed that these structures were due to the fragments following the dissociation of background oxygen molecules. For convenience, 100eV TOF data of oxygen molecule breakup is also shown in Figure 4.6. It is obvious that the structure in D_2O TOF data is quite different from that of the O_2 dissociation, which indicates that these tiny structures at long times are contributions from some other dissociation process. A reasonable explanation for the difference between the TOF structures of H_2O and D_2O is isotopic shift of the structures. When D_2O substitutes for H_2O as target, the feature labeled "B" in H_2O TOF data shifts to longer times; on the contrary, the feature labeled "C" shifts to shorter times. These two features move toward each other and merge into a single feature, which is labeled "A" in D_2O TOF data. Therefore, an oxygen containing species provides the dominant contribution to the C feature, and the main fragment responsible for B feature is a product that only contain hydrogen element that might be metastable H or H_2, or ionic H or H_2.

From the TOF spectra, it is clear that the dominant feature is the faster primary peak. Therefore, a special attention was given to this faster primary structure. Due to the fact of fluorescence decay, the prompt photon peak is followed by a long tail, which extends toward the fragment signals. Since the faster primary feature is close to the prompt photon peak, this structure is actually a combination of the real fragment signal and the tail of the photon peak. The photon decay tail can be fitted by scaled exponential expressions.

56
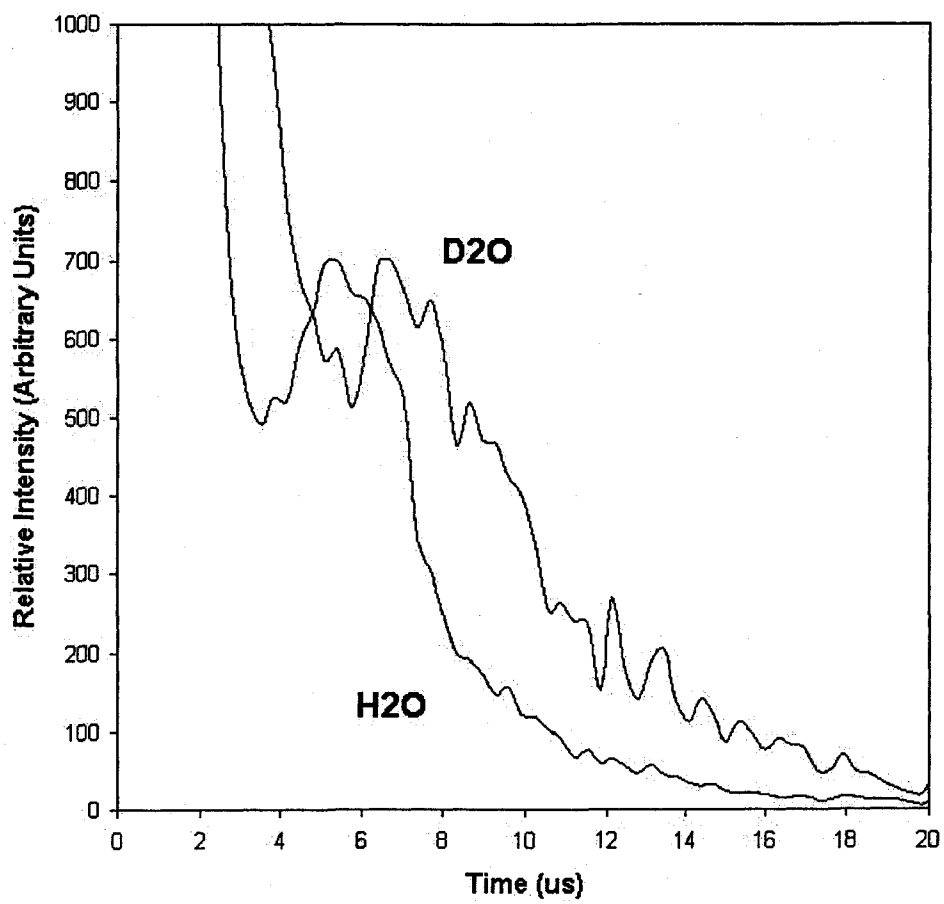
Figure 4.5. Comparison of TOF spectra for fragments produced by 100eV EID on H_2O and D_2O.
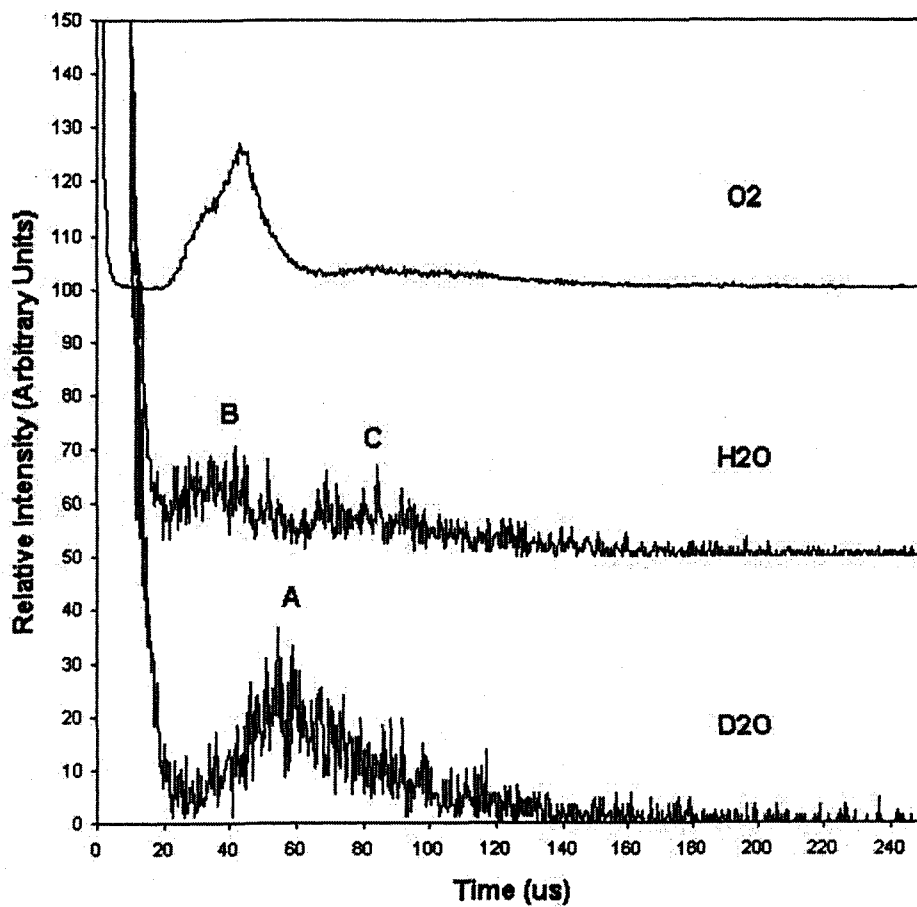
57

Figure 4.6. Comparison of TOF spectra for fragments with long flight time produced by 100eV EID on H_2O, D_2O, and O_2 on a magnified scale.
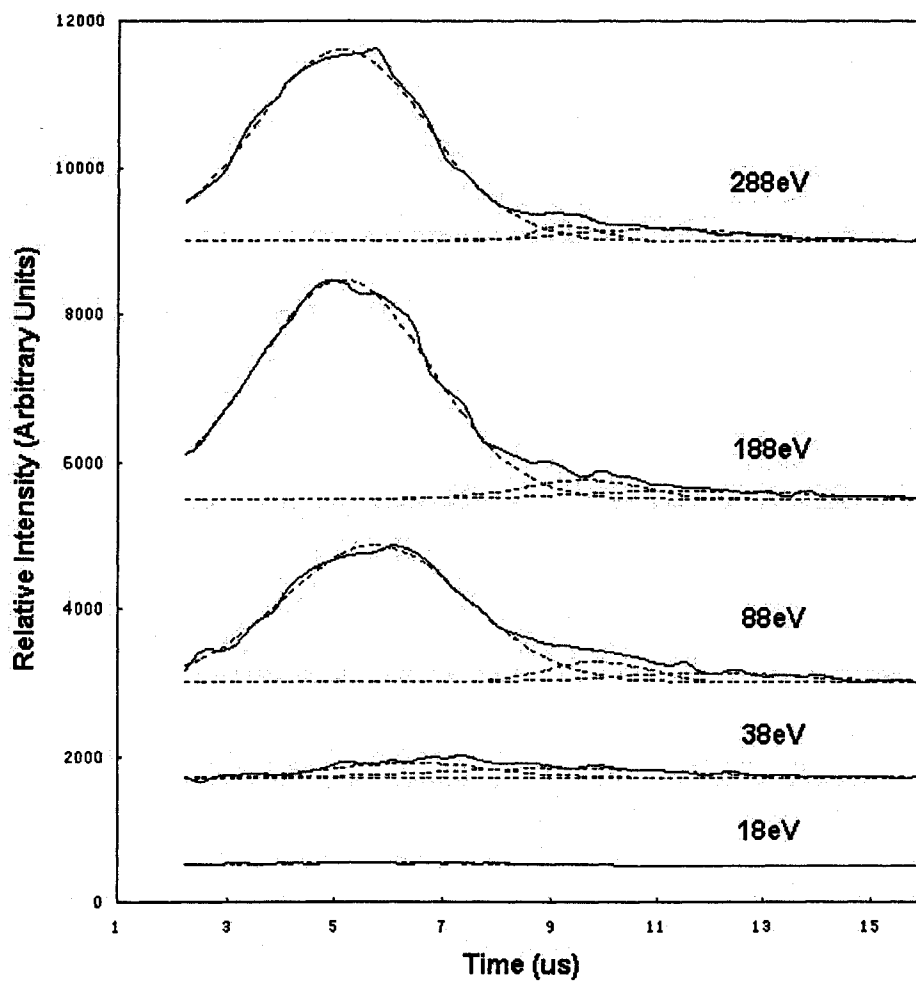
58

Figure 4.7. Corrected TOF distribution of the major peak in figure 4.1(for H_2O).
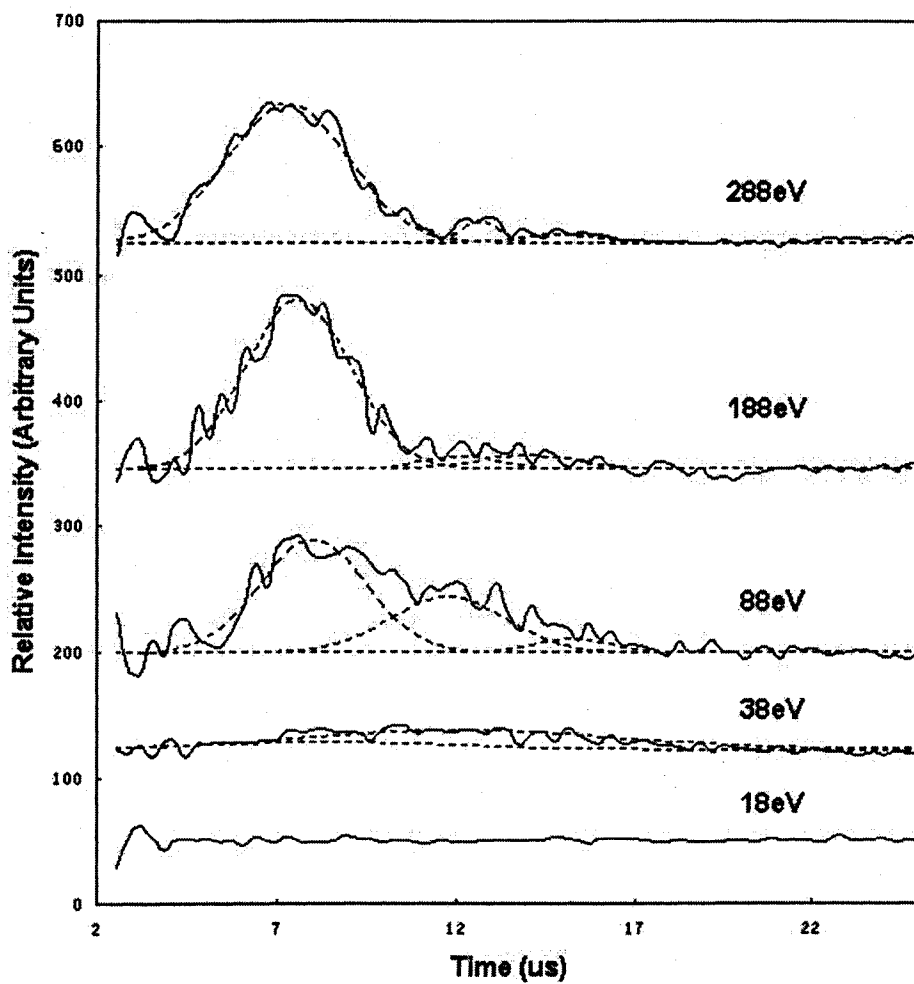
59

Figure 4.8. Corrected TOF distribution of the major peak in figure 4.3(for D_2O).

60

Subtraction of this scaled exponential fit from the original TOF data results in a set of TOF spectra of pure fragments at different impact energies, which are shown in Figure 4.7 (for H_2O) and Figure 4.8 (for D_2O). Figure 4.7 and Figure 4.8 demonstrate that an obvious feature appears only at impact energy of 38eV and above, so the threshold for this faster primary structure must be lower than this energy. To illustrate the compound nature of this faster primary structure, the TOF data are separated into several peaks by fitting the data with Gaussian functions. The dotted lines shown in Figure 4.7 (and Figure 4.8) represent these fitting Gaussian peaks. Three Gaussian distributions, centered around 5.5us, 10us, and 12us respectively, are necessary to give an excellent fit of the H_2O TOF data. The 12us Gaussian peak, however, is not visible in the 38eV TOF spectrum. As an approximation, each of these Gaussian distributions can be treated as a fragment production process. At higher impact electron energies, the faster 5.5us Gaussian peak becomes the dominant part, and the sum of the rest two Gaussian peaks only contributes as a shoulder of the faster peak. From the Figure 4.8, it is clear that the superposition of two Gaussian distributions is good enough to fit the D_2O TOF data well at impact energies of 38eV. These two Gaussian peaks are centered at approximately 8.0us and 12us, respectively. The third Gaussian fitting curve, which has a maximum at about 14.5us, is required to fit the 88eV, 188eV,and 288eV D_2O TOF spectrum. It is obvious that the fastest Guassian peak becomes much stronger as the impact energy increases from 38eV to 188eV.

We assume that the location and the FWHM of the TOF peak from a single

61

process are independent of the impact electron energy. The Gaussian fitting peaks in Figure 4.7 and Figure 4.8 are observed to shift a little bit with the increase of the impact electron energy, which means that our Gaussian distributions are not exact representatives of the real dissociation processes. However, the positions of the same peak at different energies are very close to each other, so our fitting at least provides an approximate approach to the real nature. Further fitting involves more Gaussian functions, which would require more complicated fitting process and cost goodness of fit.

Kinetic energy analysis

If the distance between the interaction region and the detector (D), as well as the mass of the detected fragment are known, the corrected TOF data and the fitting curves in Figure 4.7 and Figure 4.8 can be converted into fragment kinetic energy (FKE) distributions by the method described in chapter 2. Furthermore, released kinetic energy (RKE) data are obtained by assuming that two-body breakup process occurred. In our case, the distance D was measured to be 26.6 cm. We assume that metastable hydrogen atom or hydrogen ion is responsible for the faster primary peak. (The possible fragments for that peak will be discussed later.) The results of transformation are shown in Figure 4.9 (for H_2O) and in Figure 4.10 (for D_2O).

The released kinetic energies are mapped from time of flight by the equation [2.1] and equation [2.5]. Meanwhile, the errors in time and in the distance are propagated to the result of kinetic energies. Factors that affect the accuracy of the

62

RKE data were discussed in chapter 2. Two most significant effects come from the uncertainties of flight time and the distance of the flight path. The theory of error analysis gives the expression of the propagation of error in released kinetic energies as

$$\delta RKE = 2RKE \cdot \sqrt{(\frac{\delta D}{D})^2 + (\frac{\delta t}{t})^2} \qquad [4.4]$$

where δD is the uncertainty in measurement of distance D, which is about 0.5cm. Since the time interval for accumulating incoming particles during the experiment was set as 0.32us, the half of the time interval, which is 0.16us, is a reasonable estimate of the time uncertainty of multichannel scalar. Compared with the width of the electron pulse, this error is too small to be considered. Thus, we took the width of electron pulse 2.5us as the measurement error of time of flight (δt). The propagation of error can be calculated through equation [4.4]. It is noted that large relative error in t at relative short time range leads to huge propagation error in RKE at high energy range. From our calculation, the width of the electron pulse is the major obstacle of enhancing the accuracy of our results, especially at high kinetic energy.

Figure 4.9 displays RKE distributions at several impact electron energies as labeled in the figure transformed from the TOF data in Figure 4.7. The results of transformation from the Gaussian fitting curves in Figure 4.7 are represented as dotted lines in Figure 4.9. It should be noted that the structures at longer flight times in TOF distribution were not transformed into RKE distributions since the t^3 factor in the transformation (see chapter 2) deteriorates signal noise at region of longer flight times.
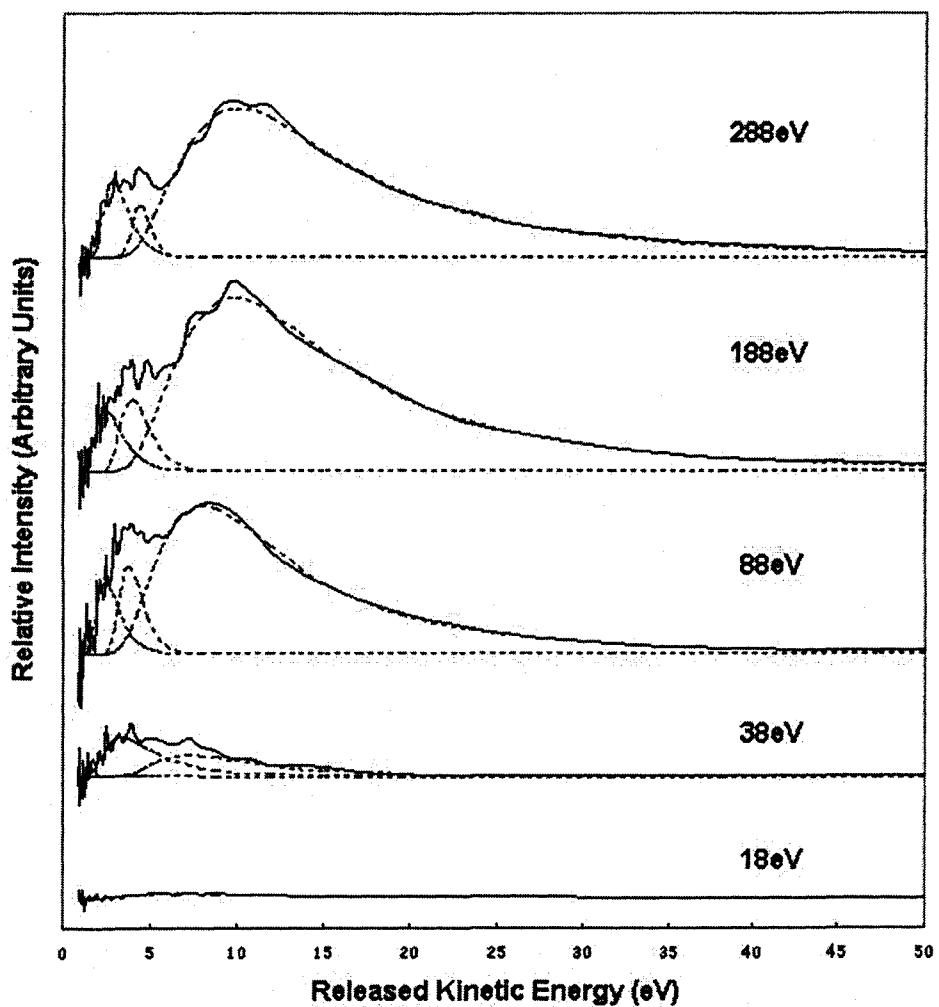
63

Figure 4.9. RKE distributions translated from the figure 4.7 (for H_2O).
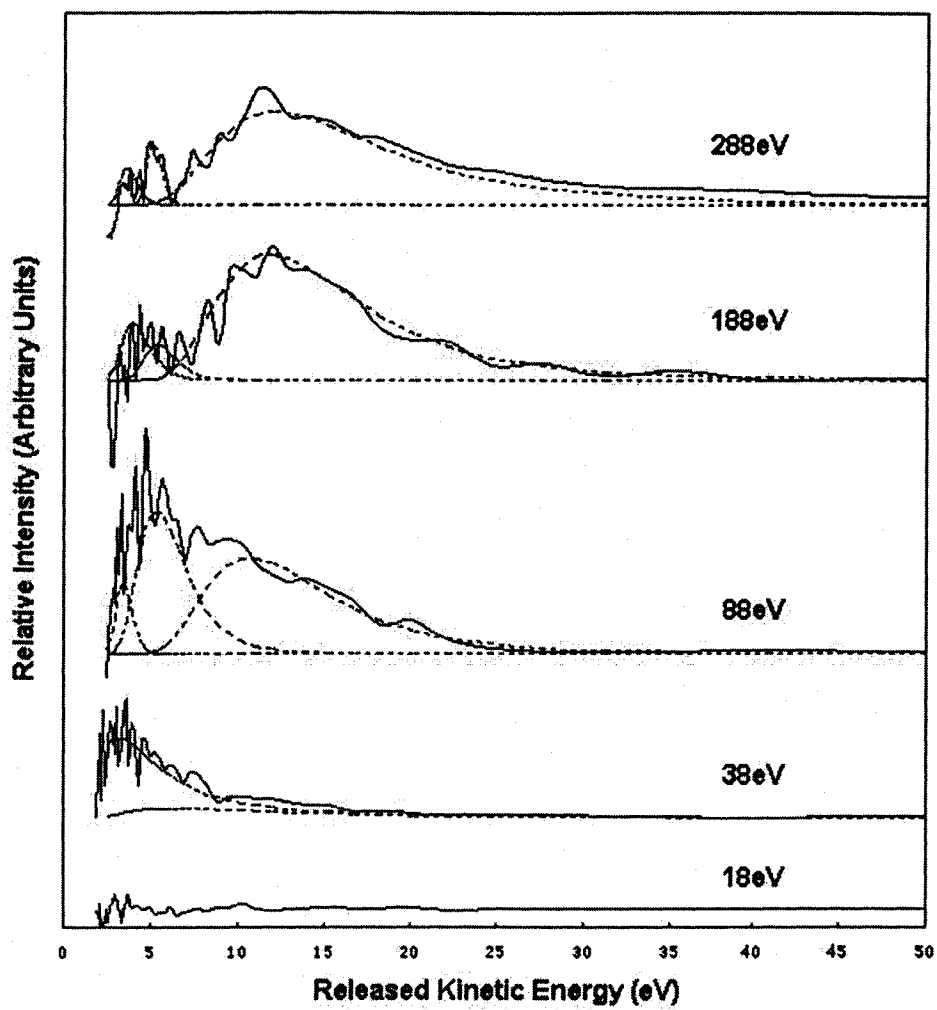
64

Figure 4.10. RKE distributions translated from the figure 4.8 (for D_2O).

65

At low incident electron energies, the intensity of the signal is relative weak and accordingly the signal-to-noise ratio is poor. Moreover, since the fitting process was introduced to estimate the possible signal peaks, the fitting curve could be broadened due to the merge of weak signal and background noise. TOF spectra (Figure 4.7 and Figure 4.8) demonstrate that the Gaussian peaks at 38eV are broader than the same peaks at higher impact energy. Due to the t^3 factor, the structure at longer flight times (lower RKE) achieves higher gain than the structure at shorter flight times (higher RKE) during the translation from TOF spectra to RKE spectra. Thus, this kind of broadening in TOF spectrum may lead to deformation of RKE spectrum and thereof a shift of the peak maximum to low RKE. This kind of shift becomes significant when impact energy is low. For example, in Figure 4.10 the first peak at 38eV and the second peak at higher impact energies are all supposed to correspond to the second Gaussian peaks in TOF data at all impact energies (Figure 4.8). Although the maximums of the TOF Gaussian peaks for different impact energies are close to each other, some of the corresponding RKE peaks shifts relative to others. In comparison with the positions of the 5eV RKE peaks at high impact energies, the same peak occurs at 3.2eV at 38eV. Due to the deformation in low impact energy RKE spectra, the distributions of RKE at high impact energies are more reliable than at low energies.

In Figure 4.9, the fitting peak near RKE of 3.5eV corresponding to the second Gaussian peak near 9.5us in Figure 4.7 provides the dominant contribution to the

66

38eV impact energy RKE distribution. As the impact electron energy increases, the feature peaked near 9eV resulted from 5.5us Gaussian peak in TOF data plays an important role more and more, and becomes the major structure. When impact energies are higher than 38eV, the third peak appears at the lowest RKE of 2.5eV. Each fitting peak appears to broaden slightly and the long tail of the highest RKE peak extends to higher values with the increase of the impact energy, which indicates that every fitting peak may be a representative of the mixture of several production channels instead of a single channel. Anther possible explanation for the long tail of the highest energy peak is that the inner repulsive potential energy curve has a steep rise at one edge of the Franck-Cordon region.

The D_2O TOF data and their fitting Gaussian curves in Figure 4.8 were converted to RKE distributions shown in Figure 4.10. Only the structure at faster flight times in the TOF spectrum were transformed into RKE spectrum. The shape of the D_2O RKE spectrum and the shape of the H_2O RKE spectrum are similar. At lower impact electron energies, the structures corresponding to long flight time peaks in TOF spectrum are the major elements of the RKE distributions. By comparing the RKE spectra of D_2O at 88eV impact energy with the RKE spectra of H_2O at the same impact energy, it is clear that the peak at approximately 5.2eV in Figure 4.10 provides more contribution to D_2O RKE data than the peak near 3.7eV in Figure 4.9 does to H_2O RKE data. At higher impact electron energies, the major feature is peaked at roughly 12eV that corresponds to 7.5us TOF feature. The lowest RKE peak is located at about 3.7eV, which dose not appears in 38eV RKE spectra. The fitting peaks are

67

also observed to shift and broaden as the impact energy changes. The long tail of the highest RKE feature extends to higher value more obviously with the increase of the impact energy than the long tail in H_2O data does.

Excitation Function

From the previous discussion, it is known that the windowed excitation function is obtained by plotting the yield of the fragment in a narrow TOF interval as a function of the impact electron energies. In the D_2O case, the Figure 4.3 demonstrates that the feature right after prompt photon signal is the major structure of the TOF distributions. Therefore, the time window, from 5us to 10us, was set to obtain the excitation function for that feature; meanwhile, another time window is opened for the excitation function of the prompt photon signal as reference. The cathode voltage was swept from 0eV to 300eV and one sweep was generally composed of 100 successive voltage steps, each of which lasted about 60 seconds. The experiment conditions (like the width and the frequency of the pulse and the head pressure of the needle) were maintained the same as in the acquisition of TOF spectra.

Obtaining the accurate identification of the threshold energy is an important purpose of the analysis of the excitation function. The energy scale of the excitation function was obtained by directly measuring the voltage bias on the filament. However, the collision energy of the electrons was not simply calculated from the voltage on the filament because contact potentials and space charge will affect the actual energy of the electron [46]. The electron energy scale calibration, therefore,

68

becomes an indispensable step of analyzing the excitation function. One reliable means of calibrating the energy scale is to observe some known threshold process of a different atom or molecule under the conditions applied for obtaining the excitation function of the molecule under study. Some special optical emission spectra of H_2 show sharp thresholds that are suitable as references. The threshold of H_α emission (656nm) from H_2 is well known at 16.6eV. Therefore, hydrogen gas was chosen as target and a 656nm filter was employed for calibration procedure in our experiment. The energy scale was amended by comparing the known threshold of 16.6eV with the threshold observed with the filter, which was placing in front of the photomultiplier. In Figure 4.11 and Figure 4.12, the excitation functions are shown on the calibrated electron energy scales.

Figure 4.11 shows the excitation functions for prompt photon. The excitation function for the particles, which falls in our definite time interval (5us~10us) corresponding to the major feature in Figure 4.3, is illustrated in Figure 4.12. It has been discussed in previous section that this major feature cannot represent the real fragment signal owing to the effect of the long tail of the prompt photon peak. In other words, the particles that arrive at detector in that time window are not only the fragments of the dissociation process but also the delayed prompt photons. This superposition of fragments and photons make all physical meanings (like threshold energy, relative values of the cross section and so on) involved in the excitation function ambiguous. In order to eliminate the interfering photon decay process, a manual procedure has to be performed to plot real excitation function for pure
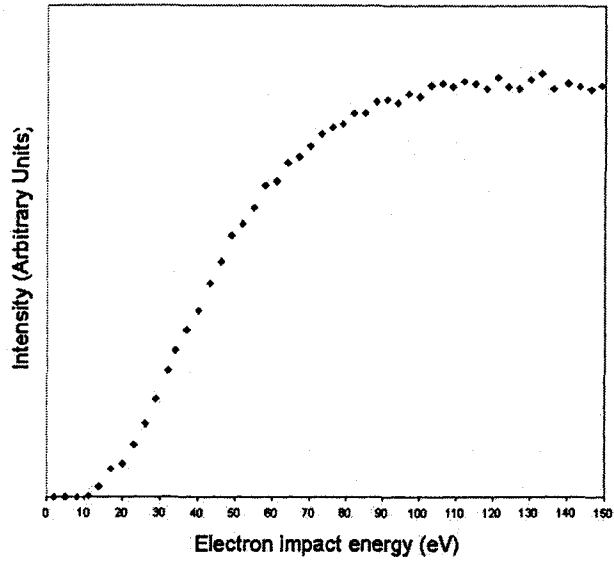
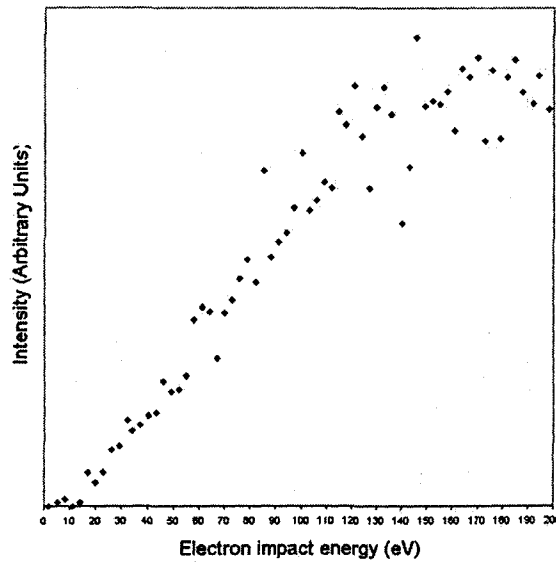**Figure 4.11.** The excitation function for prompt photon produced by EID of D₂O.

Figure 4.12. The excitation function for the particles with TOF from 5us to 10us produced by EID of D₂O.

70

fragment signal. In this procedure, the excitation function for the prompt photon was used as reference since the prompt photon peak in any TOF spectrum is clear and pure. Firstly, a set of TOF spectra corresponding to a set of different electron impact energies had to be acquired under the same condition as when the photon excitation function was measured. Secondly, the TOF distributions for pure fragment at different electron impact energies were distilled from each original TOF spectrum by subtraction of the exponential fitting curves of the decrease slope of the photon peaks just as we have seen in last section. If it is assumed that the intensity of photon signal is related to the intensity of each fragment signal linearly in the TOF spectrum, then the excitation function of the pure fragment signal can be estimated on the basis of the excitation function of prompt photon. Finally, we scaled the photon signal intensity in each impact energy TOF data suitably so that its value matches the value of photon excitation function at the same energy, and then adjust the fragment signal intensity in proportion. The result turns out to be the value of the pure fragment excitation function at the corresponding energy. A set of these discrete values represents the tendency of the excitation function. Since this method needs to acquire TOF spectrum at each of chosen electron energies and analyze these TOF data one by one manually, it is impossible to sweep 100 different electron impact energies like program controlled photon counter (SR400) does. To avoid much more calculation we only picked up a few impact energies to analyze corresponding TOF data, however this leaded to an excitation function with poor accuracy. The Figure 4.13 exhibits that

excitation function of pure fragments arriving at detector between 5us to 10us constructed by this manual procedure. The curves between known data points were constructed by using interpolation process. Since the increments of chosen energies were relatively small at low energy region, the low energy data were fitted using a shape-preserving (Piecewise cubic Hermite interpolation, PCHIP) interpolation, which preserved monotonicity and the shape of the data. At high energy region, cubic spline interpolation was employed for the data with relatively large energy increment. During the fitting process, three unreliable data were excluded.

Because the electron energy spread due to the voltage drop across the filament is about 2eV and the electron energy spread due to thermionic emission from filament surface is about 2eV(see Chapter 3), the electron energy scale is uncertain by about ± 2eV. Another considerable aspect for the uncertainty of the threshold is the increment of the swept energies for getting excitation function. Although extrapolation of the fitting curve to zero can evaluates the threshold, the result is just an approximate value. It is difficult to locate the threshold exactly in the region between the energy settings above and below a threshold. Thus, the uncertainty can be taken as the half of the division of two successive energy settings between which the threshold falls. Until now, we have talked about two kinds of uncertainty among which the larger one can be taken as the final error of the threshold.

It has been mentioned in previous chapter that an excitation function sometimes does not change smoothly, but shows sharp turns (breaks) at some voltages. Each of these breaks corresponds to a threshold for an individual dissociation process.

72

It is evident from Figure 4.13 that there are two breaks in the excitation function curve.
Straight-line approximation was used to the first two dots and the energy intercept of
this line is treated as the first threshold. The curve rises from zero at the first threshold
near 12.5eV to a broad peak around 115.5eV and then falls slowly. The gradual onset
is followed by two breaks that occur at approximately 23eV and 58eV respectively.
Two obvious breaks indicate that there are at least three dissociation processes
contributing to the major peak in D_2O TOF spectra, which agrees with the result from
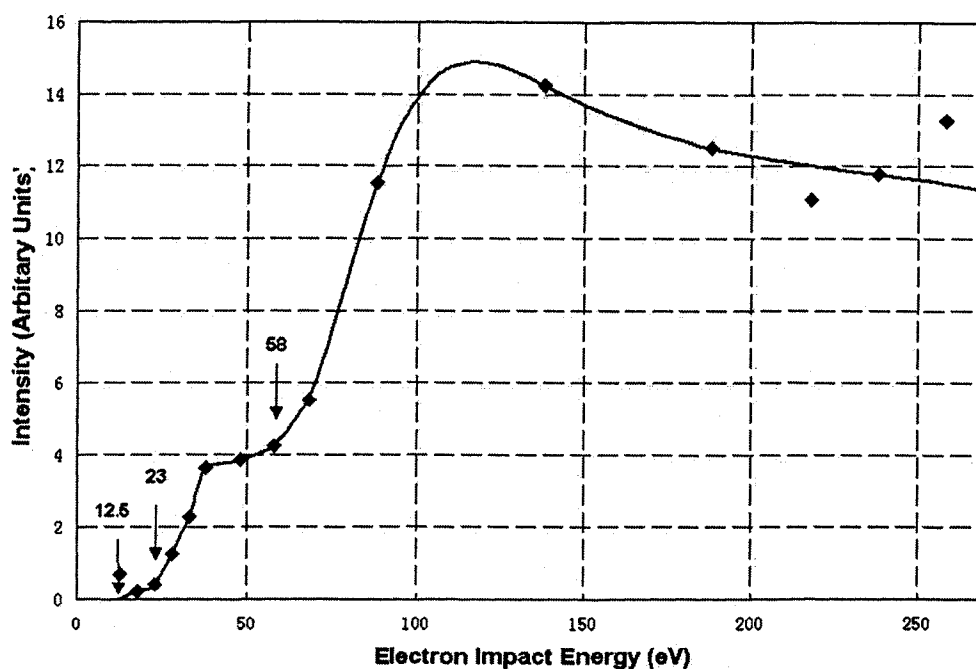the resolution of D_2O TOF spectra.

Figure 4.13. The excitation function for the pure fragment due to dissociation of D_2O
with TOF from 5us to 10us.

The major features of TOF spectra in Figure 4.3 are extracted in order to eliminate the effect of prompt photon and depicted in Figure 4.8. Furthermore, this major feature was resolved into three Gaussian-like structures by using curve fitting process. Figure 4.8 illustrates that the third Gaussian peak is not observable in the 38eV TOF spectrum, which indicates that the threshold at about 58eV corresponds to the dissociation process dominant in the third Gaussian structure. At 38eV incident energy the maximum of the second Gaussian peak is two and half times greater than that of the first Gaussian peak. Therefore, it is reasonable to assume the dominant process for the second Gaussian structure has the threshold at about 12.5eV and the dominant process for the first Gaussian structure has the threshold at about 23eV.

According to isotopic analysis, it has been known that only the ionic or the neutral metastable fragments (atom or molecule), which only contain hydrogen element, can be responsible for that major feature in Figure 4.3. If we assume the second Gaussian structure is due to the ionic or the metastable hydrogen atom, the released kinetic energy corresponding to that peak is 5.18eV. The dissociation limit is given by subtraction of the released kinetic energy from the threshold. The threshold observed in Figure 4.13 is 12.5 ± 2eV, which is close to the onset of 11 ± 2eV for the electron impact dissociation of water measured by Freund [27]. So, the dissociation limit for the process is calculated to be about 7.32 ± 2eV.

The electron attachment during the dissociation process of the heavy water can give rise to the formation of negative ions. $H^-(D^-)$ has been shown by

74

Buchel'nikova[12] and Schulz[13] to be the principal negative ion formed by electron impact in water (heavy water). The dissociation limit for the dissociation process:

$$D_2O + e \rightarrow D_2O^- \rightarrow D^- + OD$$
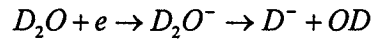
was reported to be $5.7 \pm 0.2\text{eV}$ [14], which falls just inside the uncertainty limit of our dissociation limit. Therefore, the D^- is probably responsible for the second Gaussian structure. By electron impact, water (heavy water) may also undergo dissociative ionization, which leads to the charged fragments $H^+(D^+)$, $OH^+(OD^+)$, O^+, $H_2^+(D_2^+)$, and O^{++}[19]. We are interested in the fragments that only contain hydrogen (deuterium) $H^+(D^+)$ and $H_2^+(D_2^+)$. The first dissociation limit for D^+ production has been measured by Appell and Durup [17] to be $18.7 \pm 0.5\text{eV}$, which is obviously out of the uncertainty region of our measured dissociation limit. The second peak cannot be due to D_2^+ either on the ground that the dissociation limit for D_2^+ production is even greater than that for D^+ production.

As we all know, the principal ionization potential for water is 12.6eV. It is interesting to note that the first threshold ($12.5 \pm 2\text{eV}$) for our excitation function is much close to that value. There is another probability that the particles reaching the detector are electrons ejected from neutral heavy water molecules under a hypothesis of symmetric ionization. Since the mass of the electron is much less than that of atom, according to equation [2.1] and equation [2.5], the kinetic energy of the electron, which is equal to the total released kinetic energy, is so small that it can be neglected. Therefore the threshold and the dissociation limit have the same value. Our measured threshold may be viewed as the ionization potential. However, the consequence of

75

light mass of the electron is that the electron should be dissociated from the neutral molecule with relative high velocity. From previous analysis, we know the first threshold corresponds to the second Gaussian peak in TOF data. The velocity related to that peak seems not to be high enough and thereby the first threshold is unlikely to associate with a process of ionization of heavy water.

Another possible particle that is responsible to the TOF structure is the metastable hydrogen (deuterium) atom H(2s) (D(2s)). The first threshold at about 12.5eV probably corresponds to a D(2s) dissociation process described by Freund [27]. In this process, the heavy water is first dissociated into the ground states of D and OD, and then D atom is excited to the metastable state of 2s, which is expressed as:

$$D_2O + e \rightarrow D(1s) + OD(X^2\Pi) \rightarrow D(2s) + OD(X^2\Pi)$$
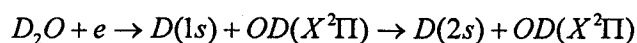
The threshold for overall process is at 10.2eV, which is just a little bit less than lower uncertainty limit of our first threshold ($12.5 \pm 2eV$).

The second threshold appears at $23 \pm 2eV$. The most possible structure in TOF data corresponding to this threshold is the first fitting Gaussian peak in Figure 4.8 (see previous discussion), which is correlated with the released kinetic energy of 11.57eV under the assumption that the peak is due to the fragment containing only one deuterium atom. If the observed fragment was the ionic or the metastable deuterium molecule, the released kinetic distribution mapped from that TOF data would peak at about 26eV. Since this is greater than our threshold, the production of deuterium molecule is clearly impossible. From the known threshold and the released kinetic

76

energy, the dissociation limit for the formation of deuterium atom was calculated to be $11.43 \pm 2\text{eV}$. Dissociation to $D(2s) + OD(X^2\Pi)$ has the dissociation limit at 15.3eV, which is just outside the rather large uncertainty.

There is an indication in Figure 4.13 that, in the vicinity of a relative high energy of 58eV, a new dissociation channel opens. The process that is identified to correspond to this threshold is the third Gaussian peak in TOF spectrum (Figure 4.8). If it is assumed that one-deuterium-containing fragment is responsible for the peak, the correlated released kinetic energy is obtained to be about 3.69eV, which is very close to the kinetic energy of 3.7eV for metastable $H(2s)$ reported by Clampitt [26]. However, there appears to be significant disagreement with the results of Clampitt. Our measured threshold is much larger than his reported threshold of 19eV for $H(2s)+OH$. We cannot presently determine this observed particle just on base of our data. It must be checked by further experiment.

Conclusions

Time-of-Flight spectroscopy was used to study the fragmentation of H_2O and D_2O following electron impact. By comparison between TOF spectra from H_2O and D_2O, isotopic shifts were observed. Under the hypothesis of two-body dissociation or symmetric three-body dissociation, substitution of deuterium for hydrogen can make peaks in TOF data due to oxygen-containing fragments shift to shorter flight times and peaks due to fragments only containing deuterium element shift to longer flight time. By analysis of isotopic shifts, the major peak in our TOF spectrum was

determined to correspond to the fragments only containing hydrogen. In addition, deconvolution of the major peak into three separate Gaussian-like structures has been illustrated.

The excitation function related to the major peak in D_2O TOF data has been studied over the range from 0eV to 300eV. At least three different production mechanisms have been identified. The onset energy was found to be 12.5±2eV, which agreed with the work of Freund. The possible dissociation processes for this threshold are:

$$D_2O + e \rightarrow D_2O^- \rightarrow D^- + OD$$

or

$$D_2O + e \rightarrow D(1s) + OD(X^2\Pi) \rightarrow D(2s) + OD(X^2\Pi)$$
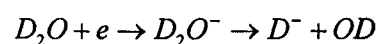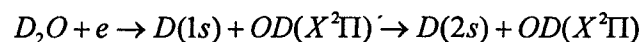
Further research is required to determine which one is the right one.

The second threshold occurred at 23 ± 2eV. If the detected fragment was production of deuterium atom, the dissociation limit turned out to be 11.43 ± 2eV, which was close to the dissociation limit (15.3eV) of the process:

$$D_2O \rightarrow D(2s) + OD(X^2\Pi)$$
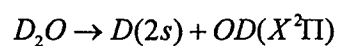
The third threshold was found to be about 58eV. This threshold probably was due to high Redberg state of deuterium, which must be check by further experiment.

Chapter 5

H_2O_2 Results

Figure 5.1 shows several time-of-flight distributions yield at different electron impact energies by using hydrogen peroxide as target. All spectra in this figure were due to the fragments following a 2.5us pulsed electron beam, which maintains a period of 1000us. The electron current collected at Faraday cup was kept about 0.3uA for the impact energy from 18eV to 300eV. At each impact energy the experiment has been running as long as others to obtain TOF data. The head pressure of the target vapor was fixed approximately 2.5torr. But, it should be noted that our source used for evaporation is actually a concentration of 30% aqueous solution of H_2O_2. The solution, therefore, raised a mixture of water and hydrogen peroxide vapor. Fortunately, Raoult's Law is a possible way of obtaining equilibrium vapor pressures of the components of an ideal solution. This allowed us to estimate the head pressures of H_2O and H_2O_2. The ratio of pressure of H_2O_2 to pressure of H_2O was about 0.009 for concentration 30% aqueous solution of H_2O_2 at temperature of 28°C (see Appendix for detail of calculation). That meant the water content was the dominant component of the gas mixture. Relative low pressure of H_2O_2 brought the trouble that the signal of H_2O_2 was very weak relative to signal of H_2O produced simultaneously.
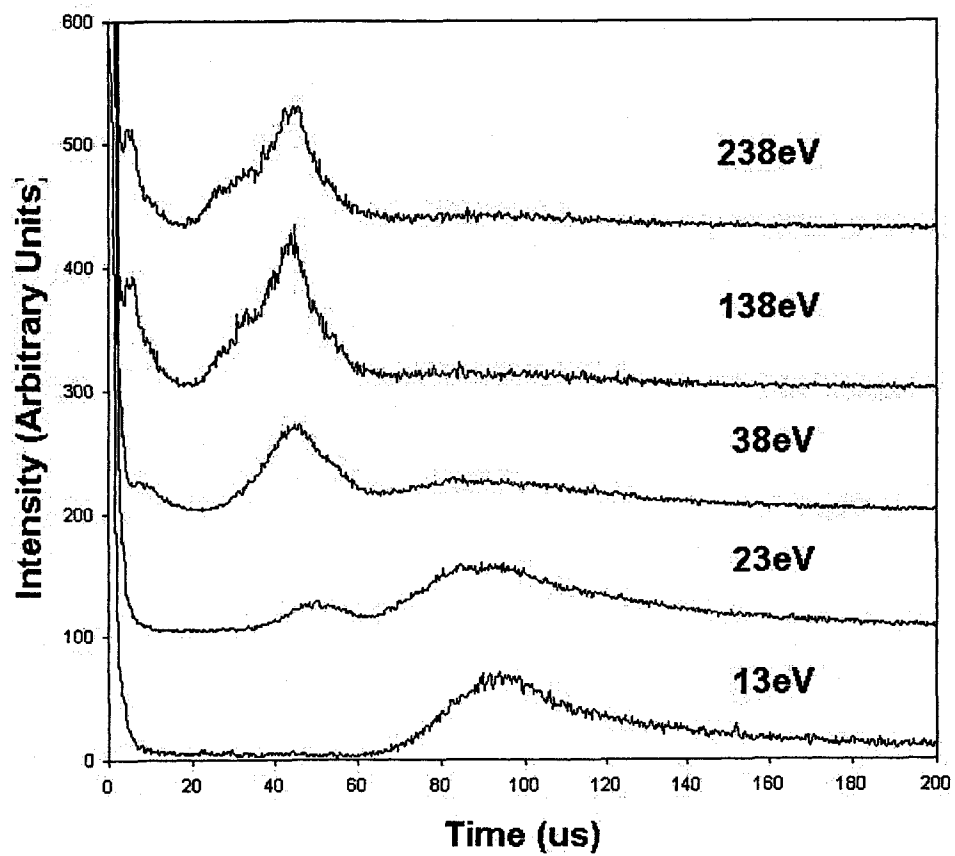
79

Figure 5.1 TOF spectra for H_2O_2 at electron impact energies shown in diagram.

For the convenience of viewing the signal, the TOF curves are all displaced upward except for the 18eV data. The signal at very short times is due to the prompt photons that are produced by decay of excited particles when electron pulse is activated. The center of this prompt photon peak is taken as the zero of the time scale. Figure 5.1 illustrates that the pattern and intensity of the TOF signal varies significantly over our studied impact energy range. At energy of 13eV the primary feature of the TOF spectra is the peak at approximately 95us. This feature appears to decrease with increase of the impact energy. It only contributes as a shoulder at energy of 38eV, and it is barely visible at energies greater than 138eV. In 23eV energy TOF data a new structure is observed as a broad peak at around 45us. In contrast to the peak near 95us, this feature grows up with increase of impact energy until the energy of 138eV at which it is most intense. The TOF data also demonstrate that the fastest peak at about 6us, which is not present at impact energies of 23eV and 13eV, becomes apparent at higher impact energies. The maxima of all peaks do not appear to obviously shift in time with increase of impact energy. Since peaks appear or disappear with change of energy and their heights alter with energy, it is probable that more than one dissociation process are contributing to the TOF signal. Moreover, there exist the competition between these processes, and different process plays dominant role by turns at different impact energies.
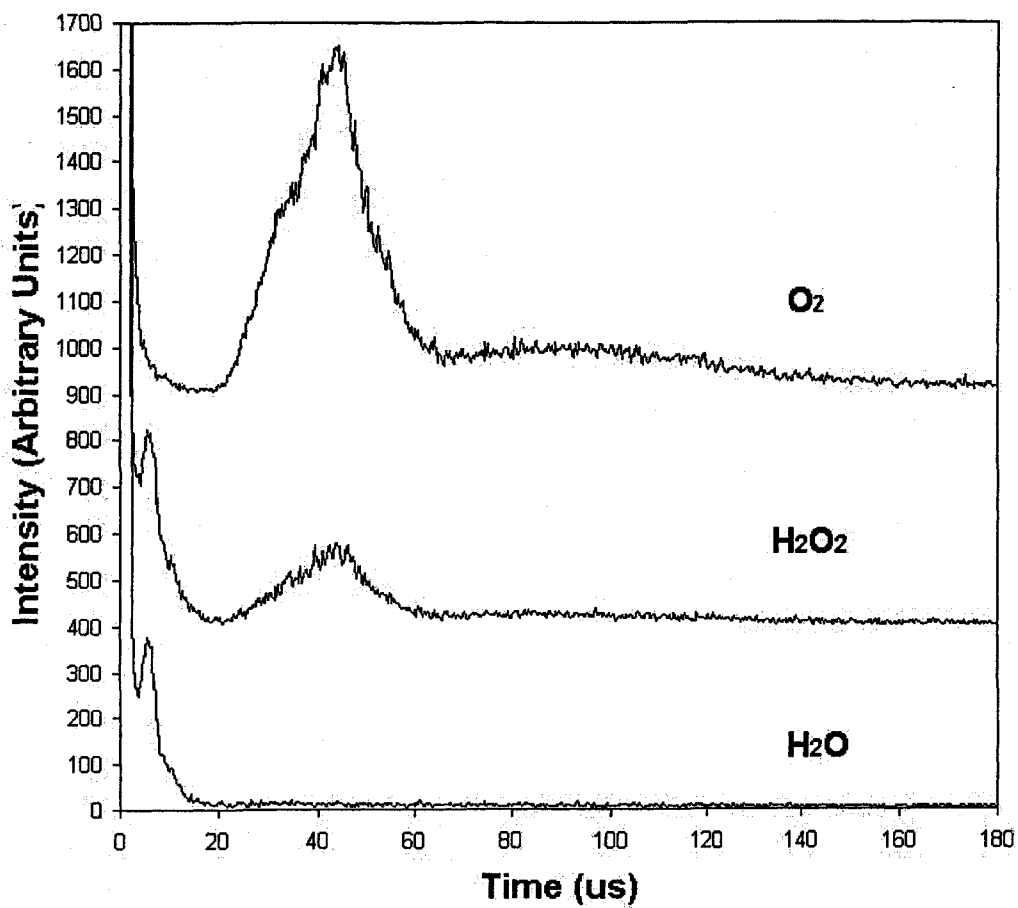
Figure 5.2 Comparison of TOF spectra for H_2O, H_2O_2, and O_2 at impact energy of 100eV.

The feature that takes place at around 6us looks familiar. It reminds us the TOF data of water (Figure 4.1) in which a peak appears almost at the same time. The peak at approximately 45us is very similar as the feature occurs in TOF of oxygen molecule. For convenience of comparison, we plotted the TOF data of H_2O, H_2O_2, and O_2 at impact energy of 100eV on one time scale as shown in Figure 5.2. All TOF spectra were obtained during the time interval with the same length and under identical conditions. It is clear that, at 100eV energy, the TOF data of H_2O_2 is actually the mixture of TOF data of H_2O and TOF data of O_2. It is not a surprise that the features of H_2O appear in TOF data of H_2O_2. We have discussed above that the water content is much more than hydrogen peroxide content in vapor mixture evaporate from concentration 30% aqueous solution of H_2O_2. By comparing with TOF spectrum of O_2, the peak occurred at around 45us is obviously due to the dissociation of oxygen molecule. A possible interpretation for the source of oxygen molecule is the decomposition of the hydrogen peroxide:

$$2H_2O_2 \rightarrow 2H_2O + O_2.$$
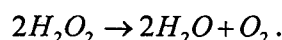
Even though part of H_2O_2 decomposes into O_2, the signal due to O_2 should not be strong since the H_2O_2 content is rare in vapor mixture. If we assume the intensity of the signal is proportional to the pressure of the target gas, which is linear with the gas concentration for ideal gas. Figure 5.2 illustrates that the intensity of peak at 45us for H_2O_2 is a quarter of the intensity of the peak at same time for O_2. That indicates the pressure of the O_2 is about one fourth of the total pressure, which is much greater the ratio of H_2O_2 vapor pressure to the total vapor pressure because of evaporation
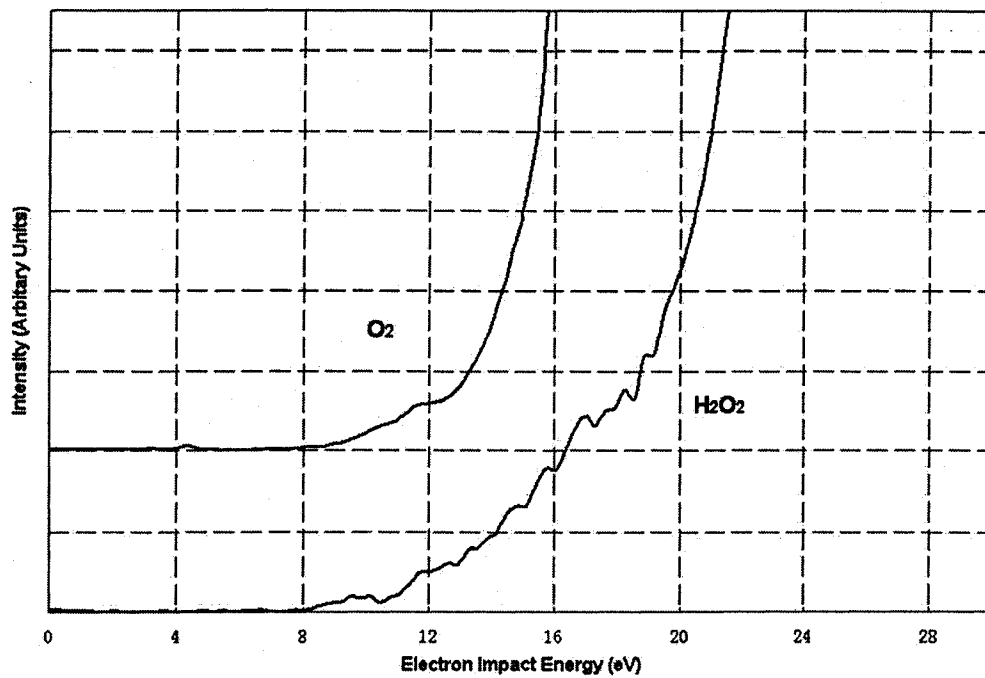
83

Figure 5.3 Excitation functions for fragmentation of oxygen and hydrogen peroxide produced by EID.

84

(see Appendix). There must be other sources providing the oxygen molecules. Oxygen impurity in the pipes due to uncompleted pumping may be a possible explanation of the extra source of the oxygen molecule.

Now, let us give some attention to the TOF spectra at low impact energy in Figure 5.1. The peak at around 95us, which appears as a shoulder in TOF data of O_2 at energy of 100eV, is the only feature at the lowest impact energy. Figure 5.2 demonstrates that our target gas is a mixture of H_2O vapor and O_2 gas. At low energies the features of H_2O do not appear, which means the dissociation of O_2 is the dominant process. Furthermore, the threshold of our experiment is supposed to be same as that of process of dissociation of O_2. Figure 5.3 shows the excitation function curves of O_2 and H_2O_2 together in one diagram. All possible TOF signals are involved in to obtain the excitation functions in this figure. It is clear that the onsets of two curves are very close: the threshold for signal from O_2 is at about 7.9eV; the threshold for signals from H_2O_2 is at about 8.2eV. This is the further proof of our earlier conclusion. If the particle responsible to the peak at 96us is assumed to be the metastable oxygen $O(^5S)$, the corresponding kinetic energy is about 0.63eV. By using two-body dissociation model, the total released kinetic energy is calculated to be 1.26eV, and then the dissociation limit is obtained as 6.94eV. We cannot presently identify the dissociation process occurred in our experiment. A more conclusive interpretation of H_2O_2 dissociation requires further research.

85

Chapter 6

Suggestion for future study

The analysis of our experimental results (TOF spectra, and excitation function) can be preformed only if the type, mass, and quantum state of the detected fragment can be identified. In actuality, it is not effective to identify the fragments fling away from the parent molecule only by using our detector, channeltron, because of the fact that channeltron is sensitive not only to the metastables of H(2s) and O(^{5}S) but also to photons, ions and some high energy Rydberg states. The usual way of distinguishing the H(2s) signal from others is to introduce quenching electric field. In the electric field, the mixture of the state 2s and 2p takes place so that the number of the H(2s) in the beam is reduced, which is accompanied by photon emission. Although two grids ,between which electric field can be formed, are mounted in front of the channeltron, they are so close to the detector that the surface of detector still cover relative large solid angle with respect to the center of the electric field. Since the photon emission due to quenching effect is supposed to be spherical symmetry, relative large solid angle of detector surface cause sufficient photons, which correspond to the metastable H(2s), to be captured by detector. By comparing with the signals with quenching field off, the signal of H(2s) cannot be removed completely by quenching field. Therefore, we suggest placing a pair of extra plates far away from the channeltron, which can form a weak electron field perpendicular to the line of sight.

86

This field combining the field right before the detector can help us identify the negative ion, positive ion, and metastable H(2s).

In chapter 4, much effort was made to remove the effect of the long tail of prompt photon signal and to distinguish a signal corresponding to a dissociation process from a convolved signal. Moreover, since signals for different fragments have merged together, it is impossible to obtain an excitation function for a unique fragment directly. We have to estimate the excitation function from TOF spectra. The complicated calculation limits the number of the TOF spectra involved in this estimation so that the accuracy of the estimated excitation function is low. One possible solution of improving the resolution of each fragment signal is to narrow the width of the electron pulse. Shorter electron pulse can restrain the spread of the TOF spectra and thereby result in relative sharp fragment peaks. Short electron pulse has another advantage of reducing the error in RKE corresponding to short flight time as discussed in chapter2 and chapter 4. Thus, in the future, it is desired that the electron pulse control could be modified to produce shorter pulse. As consequence of this modification, the effect of long photon decay tail on the signal with short TOF could be attenuated and the fragment signals, which used to be mixed, may distinguish themselves from others. Additionally, the accuracy of RKE data could be improved, especially for that corresponding to short flight time.

Analyses of the results of H_2O_2 demonstrated that our attempt of investigating the electron impact dissociation process of H_2O_2 failed. The reason is that relative low concentration (30%) water solution of H_2O_2 was used as the source of vapor. Vapor

87

pressure of H_2O_2 is much lower than that of H_2O so that the signal from dissociation of H_2O_2 is too weak to be detected. In addition, we found the signal of the O_2 dissociation, which indicates that the spontaneous decomposition may occur during the experiment. We suggest using high concentration solution to repeat this experiment, and substituting glass made pipes for stainless steel made pipes in order to lower the probability of spontaneous decomposition.

References

[1]. D.A. Vroom and F.J. de Heer, J. Chem. Phys. 50, 1883 (1969).

[2]. N. Böse and W. Sroka, Z. Naturforsch. 28a, 22 (1973).

[3]. C.I.M. Beenakker, F.J. de Heer, H.B. Krop, and G.R. Möhlmann, Chem. Phys. 6, 445 (1974).

[4]. N. Kouchi, K. Ito, Y. Hatano, N. Oda, and T. Tsuboi, Chem. Phys. 36, 239 (1979).

[5]. T. Ogawa, N. Yonekura, M. Tsukada, S. Ihara, T. Yasuda, H. Tomura, K. Nakashima, and H. Kawazumi, J. Phys. Chem. 95, 2788 (1991).

[6]. C.M. Lawrence, Phys. Rev. A2, 397 (1970).

[7]. C. Hayakawa, Proc. Phys. Math. Soc. Japan. 26, 78 (1944).

[8]. S. Tsurubuchi, T. Iwai and T. Horie, J. Phys. Soc. Japan. 36, 537 (1974).

[9]. H. Kawazumi, and T. Ogawa, Chem. Phys. 114, 149 (1987).

[10]. M. Darrach and J.W. McConkey, Chem. Phys. Lett. 184, 141 (1991).

[11]. T. Harb, W. Kedzierski, and W. McConkey, J. Chem. Phys. 115, 5507 (2001).

[12]. I.S. Buchel'nikova, Zh. Eksperim. i Teor. Fiz. 35, 1119 (1958). [English transl.: Soviet Phys.—JETP. 8, 783 (1959)].

[13]. G.J. Schulz, J. Chem. Phys. 33, 1661 (1960).

[14]. R.N. Compton, and L.G. Christophorou, Phys. Rev. 154, 110 (1967).

[15]. J. Schutten, F.J. de Heer, H.R. Moustafa, A.J.H. Boerboon, and J. Kistemaker, J. Chem. Phys. 44, 3924 (1966).

[16]. H. Ehrhardt, and A. Kresling, Z. Naturf. 22a, 2036 (1967).

[17]. J. Appell, and J. Durup, Int. J. Mass Spectrom. Ion Phys. 10, 247 (1972/73).

[18]. R.B. Cordaro, K.C. Hsieh, and L.C. McIntyre Jr, J. Phys. B: At. Mol. Phys. 19, 1863 (1986).

[19]. J.J. Olivero, R.W. Stagat and A.E.S. Green, J. Geophys. Res. 27, 4797 (1972).

[20]. S. Trajmar, D.F. Register and A. Chutjian, Phys. Rep 97, 219 (1983).

[21]. K.Niira, J. Phys. Soc. Japan. 4, 230 (1949).

[22]. K.Niira, J. Phys. Soc. Japan. 7, 193 (1952).

[23]. K.J. Laidler, J. Chem. Phys. 22, 1740 (1954).

[24]. J.C. Leclerc, J.A. Horsley, and J.C. Lorquet, Chem. Phys. 4, 337 (1974).

[25]. C.R. Claydon, G.A. Segal, and H.S. Taylor, J. Chem. Phys. 54, 3799 (1971).

[26]. R. Clampitt, Phys. Lett. 28A, 581 (1969).

[27]. R.S. Freund, Chem. Phys. Lett. 9, 135 (1971).

[28].W. Kedzierski, J. Derbyshire, C. Malone, and J.W. McConkey, J. Phys. B: At. Mol. Opt. Phys. 31, 5361 (1998).

[29]. G. Allcock and J.W. McConkey, Chem. Phys. 34, 169 (1978).

[30]. H. Bethe, Ann. Physik 5,325 (1930).

[31]. M. Inokuti, Rev. Mod. Phys. 43, 297 (1971).

[32]. U. Fano, Phys. Rev. 95, 1198 (1954).

[33]. V.I. Ochkur, Soviet Phys. J.E.T.P. 18, 503 (1964).

[34]. I.D. Latimer and J.W. McConkey, Proc. Phys. Soc. 86, 745 (1965).

[35]. L.R. LeClair, "Production and Detection of Metastable Atomic Oxygen". Ph.D. thesis, University of Windsor (1993), Chapter 3.

[36]. S. Trajmar and J.W. McConkey, "Adv. At. Mol. Opt. Phys." Ed M Inokuti, Academic Press, NY (1993).

[37]. E.C. Zipf, Electron-Molecule Interaction and their Application 1, Academic Press, NY (1984).

[38]. N.J. Mason and W.R. Newell, J. Phys. B22, 2297 (1989).

[39]. C.P. Malone, 'Electron-cluster Interaction: Excitation of Neutral Fragment in Rare Gas and Simple Molecules" PhD thesis. University of Windsor (2003).

[40]. M. Misakian, M.J. Mumma, and J.F. Faris, J. Chem. Phys. 62, 3442 (1975).

[41]. J.J. Corr, M.Sc. Thesis, University of Windsor (1987).

[42]. J.M. Ajello, et al. Appl. Opt. 27, 890 (1988).

[43]. L.R. LeClair, "Production and Detection of Metastable Atomic Oxygen". Ph.D. thesis, University of Windsor (1993), Chapter 4.

[44]. F.H. Field and J.L. Franklin, "Electron Impact Phenomena", Academic Press, NY (1970).

[45]. Karras, William Leslie, thesis, University of Windsor (1988).

[46]. D.W.O. Heddle, Proc. Phys. Soc. London 90, 81 (1967).

Appendix

The relationship between saturated H_2O_2 and H_2O vapor

The purpose of this appendix is to generalize the method reviewed by Schumb [A-1] for calculating equilibrium vapor pressure and composition of hydrogen peroxide-water mixture.

Let us firstly consider the situation of pure substance. The saturated water vapor pressure given by Keyes [A-2] can be expressed in denary logarithm form as

$$\log_{10} P_w^o(T) = G + A/T + B\log_{10} T + CT + DT^2 + ET^3 + FT^4 \qquad \text{[A-q-1]}$$

where T is the absolute temperature, A=-2892.3693, B=-2.892736, C=-4.9369728e-3, D=5.606905e-6, E=-4.645869e-9, F=3.7874e-12, and G=19.3011421. For the saturated vapor pressure of H_2O_2, the similar expression was derived by Scatchard et al [A-3]. That is,

$$\log_{10} P_H^O(T) = D + A/T + B\log_{10} T + CT \qquad \text{[A-q-2]}$$

where A, B, C, and D are constants, A=-4025.3, B=-12.996, C=4.6055e-3, and D=44.5706.

For the situation of solution made up of volatile materials, Raoult's law is helpful to find the vapor pressure of components to the composition of the solution. The law states that the vapor pressure of each component is proportional to its mole fraction, and the proportionality constant is simply the vapor pressure of the pure

92

component. In mathematical form, it is expressed as

$$P_i = P_i^o x_i \qquad \text{[A-q-3]}$$

where P_i is the vapor pressure of component i , P_i^o is the vapor pressure of componet i when it is pure, x_i is the mole fraction of component i in the solution. Unfortunately, because of the bond formed between H_2O_2 and H_2O molecules, Raoult's law cannot be directly used for aqueous solution of hydrogen peroxide. An activity coefficient, r_i, has to be introduced to modify the equation [A-q-3]:

$$P_i = P_i^o x_i r_i \qquad \text{[A-q-4]}$$

Scatchard *et al* calculated the activity coefficients for water and hydrogen peroxide [A-3]. They are given by

$$r_w = \exp\{\frac{(1-x_w)^2}{RT}[B_0 + B_1(1-4x_w) + B_2(1-2x_w)(1-6x_w)]\} \quad \text{[A-q-5]}$$

and

$$r_h = \exp\{\frac{x_w^2}{RT}[B_0 + B_1(3-4x_w) + B_2(1-2x_w)(5-6x_w)]\} \qquad \text{[A-q-6]}$$

where the subscripts w and h refer to water and hydrogen peroxide respectively. x_w is the mole fraction water in solution, R is the universal gas constant. $B_0 = -1017 + 0.97T$, $B_1 = 85$, and $B_2 = 13$. The equation [A-q-5] actually involves the fact that the sum of the mole fraction of the components in solution must be unity, $x_h + x_w = 1$. If we assume the vapors are ideal gases, according to Dalton's law, the total vapor pressure above the solution is equal to the sum of the vapor pressure of components, $P_{tot} = P_h + P_w$.

The vapor pressure we are talking about is the pressure of vapor in equilibrium with the liquid. It is not the head pressure we measured in experiment. Ejection of

93

target gas through capillary could be treated as the process of throttle. The relative high vapor pressure in source container is reduced to relative low head pressure by throttle. In the case of gas mixture, the ratio of pressure of components before the throttle is supposed to be same as that after the throttle under the assumption of ideal gases.

In this work we used the H_2O_2 solution with a concentration of 30%, which can be translated to the mole fraction of about 0.18. If the room temperature of $28^\circ C$ is taken as T to feed into above equations, the pressures of H_2O_2 and H_2O, and the ratio of them can be calculated. The results are shown as follow.

$$P_w \approx 21.92 \quad torr$$

$$P_h \approx 0.19 \quad torr$$

$$\frac{P_h}{P_w} \approx 0.009 .$$

References

A-1. W.C. Scumb et al., Amer. Chem. Soc. Monograph (1955).

A-2. F.G.Keyes, J. Chem. Phys. 15, 602 (1947).

A-3. G.Scatchard et al., J. Am. Chem. Soc. 74, 3715 (1952).

Vita Auctoris

NAME:	Xinqing Liao
PLACE OF BIRTH:	Beijing, China
YEAR OF BIRTH:	1976
EDUCATION:	The High School attached to Tsinghua University Beijing, China 1991-1994
	Shanghai Jiaotong University Shanghai, China 1994-1998
	University of Windsor Windsor, Ontario, Canada 2003-2006